

Floquet engineering of Hilbert space fragmentation in Stark lattices

Li Zhang ^{1,2}, Yongguan Ke,^{1,2,3} Ling Lin,^{1,2} and Chaohong Lee ^{1,2,4,*}

¹*Institute of Quantum Precision Measurement, State Key Laboratory of Radio Frequency Heterogeneous Integration, Shenzhen University, Shenzhen 518060, China*

²*College of Physics and Optoelectronic Engineering, Shenzhen University, Shenzhen 518060, China*

³*Laboratory of Quantum Engineering and Quantum Metrology, School of Physics and Astronomy, Sun Yat-Sen University (Zhuhai Campus), Zhuhai 519082, China*

⁴*Quantum Science Center of Guangdong-Hongkong-Macao Greater Bay Area (Guangdong), Shenzhen 518045, China*



(Received 10 November 2023; revised 3 April 2024; accepted 6 May 2024; published 29 May 2024)

The concept of Hilbert space fragmentation (HSF) has recently been put forward as a routine to break quantum ergodicity. Although HSF exists widely in models with dynamical constraints, it is still challenging to tune it. Here, we propose a scheme to tune the HSF in a one-dimensional tilted lattice of interacting spinless fermions with periodically driven tunneling. For weak tunneling strength, the dynamics for a long range of time is governed by effective Hamiltonians with kinetic constraints, which appear as density-dependent tunneling. Through a Floquet time-dependent perturbation theory, we *analytically* derive two different resonance frequencies, at which some particular tunneling processes are resonant. At the nonresonance frequencies, the system is strongly constrained and exhibits a strong HSF. At the two different resonance frequencies, the kinetic constraints are partly released and the system exhibits another two different strong HSFs. We can tune the HSF by changing the driving frequency. We support the perturbation analysis with exact numerical simulation of the entanglement entropy, the density correlation functions, and the saturated local density profiles. Our result provides a promising way to control HSF through Floquet engineering.

DOI: [10.1103/PhysRevB.109.184313](https://doi.org/10.1103/PhysRevB.109.184313)

I. INTRODUCTION

Recently, there has been much interest in exploring whether and how an isolated quantum many-body system can reach thermal equilibrium under unitary dynamics. While ergodic systems can reach thermal equilibrium rapidly via eigenstate thermalization hypothesis [1–5], the failure of thermalization due to ergodicity breaking has been predicted in several systems [6–8]. Two well-known examples for ergodicity breakdown are quantum integrable systems and many-body localized systems, both of which possess an extensive number of conserved quantities [6,7,9–15]. Moreover, exotic violation of ergodicity has been found in systems subjected to strong tilting potentials [16–25], hosting quantum many-body scars [8,26–30] and of fractured Hilbert space [8,31–34].

Hilbert space fragmentation (HSF) describes the phenomenon that the Hilbert space of a system is split into many dynamically disjoint invariant subspaces (referred to as Krylov subspaces), which cannot be captured by conventional symmetry [8,31–35]. Thus, large parts of the Hilbert space are inaccessible to certain initial states, and the ergodicity breaks down regarding the full system. The HSF usually arises in systems with dynamical constraints [31–34,36–47], such as fractonlike constraints of conservation of $U(1)$ charge and its associated dipole [31–34], and local tunneling

constraints induced by strong interaction or strong tilting potentials [36,37,42–46]. Other examples include models with frustration [48,49]. Depending on whether the largest Krylov subspace can span almost the entire symmetry space or not in the thermodynamic limit, the HSF is categorized as weak and strong, respectively [8,32]. It can be diagnosed by the dimension ratio between the largest Krylov subspace and the symmetry space, which tends to 1 or 0 in the thermodynamic limit for weak or strong HSF [8,32]. Although the HSF can be different when changing the filling number, i.e., changing the symmetry sector [50,51], to the best of our knowledge there is still no way to control the HSF by tuning the physical parameters within a quantum number sector of a symmetry.

Floquet engineering, the coherent control of a quantum system via periodic driving, is a powerful tool for engineering synthetic Hamiltonians with novel properties [52]. It has been used to realize topological Bloch bands, dynamical localization, synthetic gauge field, etc. [52]. Specifically, density-dependent tunneling has been engineered by suitable driving schemes [52–55]. Recently, it has been proposed to generate quantum many-body scars and HSF via engineering local tunneling constraints [46,47,56]. However, these works only realize particular forms of kinetic constraint and cannot adjust the HSF.

In this article, we provide a way to tune the HSF within the half-filling sector in a periodically driven Stark chain of interacting spinless fermions. Fermions are of nearest-neighbor interaction, subjected to a tilted field and tunnel between nearest-neighboring sites with strength varying

*chleecn@szu.edu.cn

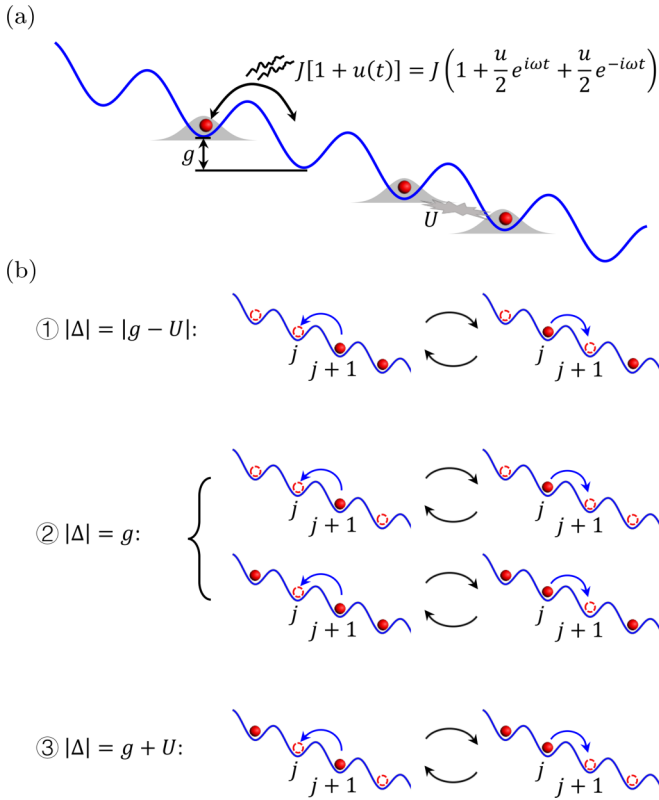


FIG. 1. (a) Schematic diagram of interacting spinless fermions in a periodically driven tilted lattice. The tilting and nearest-neighbor interaction strength are g and U , respectively. Fermions tunnel between nearest-neighbor sites with a periodically varying strength $J[1 + u(t)]$, where $u(t) = u \cos \omega t$. (b) Illustration of the three tunneling processes ①②③, which are characterized, respectively, by the projected tunnelings $\hat{\mathcal{P}}_{j-1,j+2}^{(|\Delta|)}(\hat{c}_j^\dagger \hat{c}_{j+1} + \text{H.c.})$ with energy barrier $|\Delta| = |g - U|$ (top), g (middle), and $g + U$ (bottom). The red balls denote the fermions and the red dashed circles denote the empty sites.

periodically, as depicted in Fig. 1(a). The tunneling strength is much smaller than the tilting strength, the interaction strength, and the driving frequency. There will be an energy barrier for particle tunneling, which depends on the tilting strength, the interaction strength, and the density near the tunneling sites. The tunneling is suppressed by the energy barrier, unless the energy barrier is equal to 0 or compensated by driving frequency. Tunneling processes are classified into three types according to barrier values; see Fig. 1(b). Thus, we can tune the relation among the interaction, tilting, and the driving frequency to make a particular tunneling process resonant and realize different forms of kinetic constraints. As a concrete example, we set the interaction and the tilting strength equal, for which one tunneling process is always resonant. We tune the driving frequency to selectively make the other two tunneling processes resonant. Three effective models with different forms of kinetic constraints are engineered, which display different fragmentations of the Hilbert space. We study the exact dynamic evolution of the original driven system, which shows consistent signatures of the HSF. Our result provides a route to controlled switching between different HSF within a fixed filling sector by tuning the driving frequency.

The rest of the paper is organized as follows. In Sec. II, we introduce our Floquet system and show how we can engineer effective models with different forms of kinetic constraints. In Sec. III, we analyze the splitting of the Hilbert space under the effective models, study the dynamic signatures of the HSF by the exact time evolution, and display the tuning of the HSF through changing the driving frequency. Finally, in Sec. IV, we give a brief summary of our results.

II. MODEL AND THE FLOQUET ENGINEERING OF KINETIC CONSTRAINTS

A. Model

We consider an ensemble of interacting spinless fermions in a one-dimensional Stark lattice under periodic driving; see Fig. 1(a). It is described by the Hamiltonian $\hat{H}(t) = \hat{H}_{\text{on}} + \hat{H}_J(t)$, where the on-site Hamiltonian

$$\hat{H}_{\text{on}} = U \sum_{j=0}^{L-2} \hat{n}_j \hat{n}_{j+1} - g \sum_{j=0}^{L-1} j \hat{n}_j, \quad (1)$$

and the periodic tunneling Hamiltonian

$$\hat{H}_J(t) = J[1 + u(t)] \sum_{j=0}^{L-2} (\hat{c}_j^\dagger \hat{c}_{j+1} + \hat{c}_{j+1}^\dagger \hat{c}_j). \quad (2)$$

Here, \hat{c}_j^\dagger (\hat{c}_j) creates (annihilates) a fermion at site j , and $\hat{n}_j = \hat{c}_j^\dagger \hat{c}_j$ is the particle number operator. The parameters J , g , and U are the nearest-neighbor tunneling strength, the tilting field strength, and the nearest-neighbor interaction strength, respectively. $u(t) = u \cos(\omega t)$ is periodic in time with frequency ω and amplitude u . L is the total number of lattice sites. In Appendix A, we provide a discussion of the realization of our model in a Rydberg atom platform. Our model may also be simulated by insulating two-component bosonic atoms trapped in a one-dimensional tilted optical lattice [57]. In the following study, we consider an open boundary condition and focus on the half-filling sector with particle number $N = L/2$. We consider $g > 0$, and we set $\hbar = 1$ and the energy unit as $J = 1$.

B. Engineering of kinetic constraints

The dynamics of our periodically driven system $\hat{H}(t)$ after a period is governed by the Floquet Hamiltonian

$$\hat{H}_F = \frac{i}{T} \ln \hat{F}. \quad (3)$$

Here, the Floquet operator \hat{F} is the unitary evolution operator over a period

$$\hat{F} = \mathcal{T} \exp \left[-i \int_0^T \hat{H}(t) dt \right], \quad (4)$$

with \mathcal{T} denoting time ordering. \hat{H}_F is untractable, since $\hat{H}(t)$ at different times does not commute with each other. Here, we apply the time-dependent perturbation theory (TDPT) in Floquet systems to obtain the Floquet Hamiltonian for small driving amplitudes [58,59].

In our model, when $J, uJ \ll g, U, \omega/2\pi$, and g and U are comparable, we can treat $\hat{H}_J(t)$ as a perturbation to \hat{H}_{on} .

The first-order effective Floquet Hamiltonian is derived in Appendix B. The first-order perturbation process can be understood from the following physical picture. On the one hand, since U and g are much larger than the tunnel strength, tunneling is suppressed due to the large energy barrier Δ . On the other hand, the tunneling strength can be written as $J[1 + u(t)] = J(1 + 0.5ue^{i\omega t} + 0.5ue^{-i\omega t})$. The periodic part of the tunneling can be viewed as “photons” assisted tunneling with “photon” frequency ω . So, tunneling can be stimulated if $\Delta = 0$ or $|\Delta| = \omega$, i.e., under the condition of resonance between the interaction and the tilting potential or resonance between the system and the driving. In our model, there are three different pairs of conjugate tunneling processes ①②③ characterized, respectively, by energy barriers $|\Delta| = |g - U|$, g , and $g + U$, which depend on the particle number near

the tunneling sites; see Fig. 1(b). They can be depicted by projected tunnelings $\hat{\mathcal{P}}_{j-1,j+2}^{(|\Delta|)}(\hat{c}_{j+1}^\dagger \hat{c}_j + \text{H.c.})$ with projectors

$$\begin{aligned}\hat{\mathcal{P}}_{j-1,j+2}^{(|g-U|)} &= \hat{n}_{j+2}(1 - \hat{n}_{j-1}), \\ \hat{\mathcal{P}}_{j-1,j+2}^{(g)} &= 1 - (\hat{n}_{j-1} - \hat{n}_{j+2})^2, \\ \hat{\mathcal{P}}_{j-1,j+2}^{(g+U)} &= \hat{n}_{j-1}(1 - \hat{n}_{j+2}).\end{aligned}\quad (5)$$

It is obvious that $\hat{\mathcal{P}}_{j-1,j+2}^{(|g-U|)} + \hat{\mathcal{P}}_{j-1,j+2}^{(g)} + \hat{\mathcal{P}}_{j-1,j+2}^{(g+U)} = 1$.

We can tune the relation between g , U , and ω to make the particular tunneling process resonant. To reduce flexibility, we fix $U = g$, which ensures intrinsic resonant tunneling without driving. The first-order Floquet Hamiltonian in this case reads

$$\begin{aligned}\hat{H}_F^{(1)} &= \frac{i}{T} \ln e^{-i\hat{H}_{\text{on}}T} + J \sum_j \hat{\mathcal{P}}_{j-1,j+2}^{(0)} \hat{c}_{j+1}^\dagger \hat{c}_j + \text{H.c.} \\ &+ \left\{ \frac{iJ}{T} (e^{-igT} - 1) \left[\frac{1}{g} + \frac{u(1 - \delta_{g,\omega})}{2(g - \omega)} + \frac{u}{2(g + \omega)} \right] + \frac{uJ}{2} \delta_{g,\omega} \right\} \sum_j \hat{\mathcal{P}}_{j-1,j+2}^{(g)} \hat{c}_{j+1}^\dagger \hat{c}_j + \text{H.c.} \\ &+ \left\{ \frac{iJ}{T} (e^{-i2gT} - 1) \left[\frac{1}{2g} + \frac{u(1 - \delta_{2g,\omega})}{2(2g - \omega)} + \frac{u}{2(2g + \omega)} \right] + \frac{uJ}{2} \delta_{2g,\omega} \right\} \sum_j \hat{\mathcal{P}}_{j-1,j+2}^{(2g)} \hat{c}_{j+1}^\dagger \hat{c}_j + \text{H.c.},\end{aligned}\quad (6)$$

where the first term is the effective on-site potential, $\hat{\mathcal{P}}_{j-1,j+2}^{(0)} = \hat{\mathcal{P}}_{j-1,j+2}^{(|g-U|)}$, and $\hat{\mathcal{P}}_{j-1,j+2}^{(2g)} = \hat{\mathcal{P}}_{j-1,j+2}^{(g+U)}$.

From Hamiltonian (6), we can see that some resonant tunnelings indeed occur at frequencies $\omega_1^r = g$ and $\omega_2^r = 2g$, where the effective potential energy difference is zero for the tunneling processes projected by $\hat{\mathcal{P}}_{j-1,j+2}^{(g)}$ and $\hat{\mathcal{P}}_{j-1,j+2}^{(2g)}$, respectively. We also see driving transparency at frequencies $\omega_q^t = g/q$ (with q being integers larger than 1), at which the tunneling strength for the two processes equals 0. At other frequencies, the system does not resonate with the driving. The effective Hamiltonians up to the first order in J/g are reduced to

$$\hat{H}_{\omega_q^t}^{\text{eff}} = J \sum_j \hat{\mathcal{P}}_{j-1,j+2}^{(0)} (\hat{c}_j^\dagger \hat{c}_{j+1} + \hat{c}_{j+1}^\dagger \hat{c}_j) \quad (7)$$

at the driving transparency frequencies $\omega = \omega_q^t$,

$$\begin{aligned}\hat{H}_{\omega_1^r}^{\text{eff}} &= J \sum_j \hat{\mathcal{P}}_{j-1,j+2}^{(0)} (\hat{c}_j^\dagger \hat{c}_{j+1} + \text{H.c.}) \\ &+ \frac{uJ}{2} \sum_j \hat{\mathcal{P}}_{j-1,j+2}^{(g)} (\hat{c}_j^\dagger \hat{c}_{j+1} + \text{H.c.})\end{aligned}\quad (8)$$

at the resonance frequency $\omega = \omega_1^r$, and

$$\begin{aligned}\hat{H}_{\omega_2^r}^{\text{eff}} &= J \sum_j \hat{\mathcal{P}}_{j-1,j+2}^{(0)} (\hat{c}_j^\dagger \hat{c}_{j+1} + \hat{c}_{j+1}^\dagger \hat{c}_j) \\ &+ \frac{uJ}{2} \sum_j \hat{\mathcal{P}}_{j-1,j+2}^{(2g)} (\hat{c}_j^\dagger \hat{c}_{j+1} + \hat{c}_{j+1}^\dagger \hat{c}_j)\end{aligned}\quad (9)$$

at the resonance frequency $\omega = \omega_2^r$. We note that in Hamiltonian (9), we have neglected the nonresonant tunneling process

projected by $\hat{\mathcal{P}}^{(g)}$ and the effective potential. This is because this tunneling amplitude $2J(3 - u)/3\pi$ is much smaller than the effective bias g , and the on-site potential is conserved after neglecting this tunneling. We also note that at other nonresonant frequencies away from ω_1^r and ω_2^r , the effective Hamiltonian can be approximated by Hamiltonian (7), because the strength of the nonresonant processes to the effective bias $\sim J/g$. The Hamiltonians (7), (8), and (9) have different forms of kinetic constraints and will show different HSF.

III. TUNING OF HILBERT SPACE FRAGMENTATION

In this section, we explore the tuning of HSF by controlling the driving frequency within the half-filling sector. We analyze the splitting of the Hilbert space based on Hamiltonians (7), (8), and (9), and we study the dynamic signatures of the HSF through the numerical simulation of the exact time evolution by exact diagonalization of the Floquet operator Eq. (4). The system size is set as $L = 16$ unless otherwise specified.

The bipartite von Neumann EE between a subsystem A and the rest of the system B is defined as

$$S = -\text{Tr}(\hat{\rho}_A \ln \hat{\rho}_A), \quad (10)$$

where $\hat{\rho}_A = \text{Tr}_B(|\psi\rangle\langle\psi|)$ is the reduced density matrix of the subsystem A . When evolving from a low-entangled initial state $|\psi_0\rangle$ in a finite system, the EE will saturate to a value S_∞ . If the Krylov subspace to which the initial state belongs is ergodic, S_∞ is consistent with the Page value of that subspace [37,46,60]. For a system without HSF, the Krylov subspace is trivially the symmetry sector. Adopting the procedure in Refs. [46,61], we can calculate the Page value

S_p of the half-filling sector and the Page value $S_p[\mathcal{K}]$ of a Krylov subspace \mathcal{K} . The latter is calculated via averaging the von Neumann EE of random canonical states in that Krylov subspace. We adopt a sufficiently large number of sampling to calculate $S_p[\mathcal{K}]$ so that the averaged EE changes less than 10^{-5} when increasing the sampling number by 100. In the following study, we consider the half-chain von Neumann EE, with A being the left half-chain of the system.

The infinite-temperature autocorrelation function of an operator \hat{O} is defined as $C(t) = \langle \psi_{\text{inf}} | \hat{O}(t) \hat{O}(0) | \psi_{\text{inf}} \rangle$, where $|\psi_{\text{inf}}\rangle$ is a random infinite-temperature state evenly distributed throughout the Hilbert space. It captures the spread of the operator \hat{O} and the symmetry and transport properties of the system [8]. In the following study, we consider the infinite-temperature density autocorrelation function at site j :

$$C_j(t) = \langle \psi_{\text{inf}} | [\hat{n}_j(t) - 1/2][\hat{n}_j(0) - 1/2] | \psi_{\text{inf}} \rangle. \quad (11)$$

At long times, $C_j(t)$ saturates to a value larger than the lower bound [8,32,46]

$$C_j^{(f)} = \frac{1}{\mathcal{D}} \sum_{\mathcal{K}} \frac{[\text{Tr}(\hat{P}_{\mathcal{K}} \hat{n}_j \hat{P}_{\mathcal{K}} - \frac{1}{2})]^2}{\mathcal{D}_{\mathcal{K}}}, \quad (12)$$

where $\hat{P}_{\mathcal{K}}$ is the projector to the Krylov subspace \mathcal{K} , $\mathcal{D}_{\mathcal{K}}$ and \mathcal{D} are the dimensions of \mathcal{K} and the whole Hilbert space, respectively, and the summation sums over all the Krylov subspaces. In the absence of HSF, \mathcal{K} is equal to the symmetry sector, and $C_j^{(f)} = 0$ for the half-filling case. In the presence of HSF, $C_j^{(f)}$ provides a lower bound for $C_j(t)$ [8,32,46].

When the Hilbert space of a system is fragmented, one can redefine ergodicity within the Krylov subspaces [34,62]. For an ergodic system without HSF, when evolving from an out-of-equilibrium state $|\psi_0\rangle$, the local observables should relax to the equilibrium values predicted by the ensemble of the symmetry sector. In contrast, for a system with HSF, they should relax to the equilibrium values predicted by the ensemble of the Krylov subspace to which the initial state belongs, if that Krylov subspace is ergodic. In the following, we study the evolution of local densities $n_j(t) = \langle \hat{n}_j \rangle$. For our system when $u \neq 0$, n_j will relax to 0.5 if there is no HSF. Otherwise, it will relax to the value

$$n_j[\mathcal{K}] = \frac{1}{\mathcal{D}_{\mathcal{K}}} \text{Tr}(\hat{P}_{\mathcal{K}} \hat{n}_j \hat{P}_{\mathcal{K}}), \quad (13)$$

where \mathcal{K} is the Krylov subspace to which the initial state belongs.

We find that all three Hamiltonians (7), (8), and (9) exhibit strong splitting of the half-filling sector with the dimension ratio between the largest Krylov subspace and the half-filling sector decaying to 0 in the thermodynamic limit. For Hamiltonians (7) and (9), this ratio decays exponentially with system size as in the common cases [32–34,37,40], and we call it exponentially strong HSF. For Hamiltonian (8), the ratio decays algebraically with system size, and we call it algebraic strong HSF. The main results is summarized in Table I. In the following, we will introduce the different fragmentations in detail and show how to tune them by changing the driving frequency.

TABLE I. The main results of tuning the HSF by changing the driving frequency for large values of g and at $U = g$. ① ② ③ are the three kinds of tunneling process illustrated in Fig. 1(b).

| ω | g | $2g$ | Other values |
|--------------------------------------|------------------|--------------------|--------------------|
| allowed | ①② | ①③ | ① |
| tunnelings | | | |
| splitting of the half-filling sector | algebraic strong | exponential strong | exponential strong |

A. Exponential strong Hilbert space fragmentation at nonresonant frequencies

When the driving frequency is away from the resonance frequencies ω_1^r and ω_2^r , the tunneling strength of the processes projected by $\hat{\mathcal{P}}^{(g)}$ and $\hat{\mathcal{P}}^{(2g)}$ is much smaller than the effective potential bias, and the two tunneling processes can be neglected. The effective Floquet Hamiltonian is given by Hamiltonian (7), which conserves the sum of the dipole moment and the number of pairs of occupied adjacent sites $\hat{e} = \hat{H}_{\text{on}}/g = -\sum_j j \hat{n}_j + \sum_j \hat{n}_j \hat{n}_{j+1}$. There are a total of N^2 symmetry spaces $\mathcal{S}_m^{(0)}$ in the half-filling sector with good quantum numbers $e_m = e_0 + m$, where $e_0 = \frac{-3N(N-1)}{2} - 1$ and $m = 0, 1, 2, \dots, N^2 - 2$ and N^2 .

Apart from $\mathcal{S}_0^{(0)}$, $\mathcal{S}_1^{(0)}$, $\mathcal{S}_{N^2-2}^{(0)}$, and $\mathcal{S}_{N^2}^{(0)}$ (with dimensions 2, 3, 1, and 1 for all system sizes), the other symmetry spaces fracture further into disconnected Krylov subspaces $\mathcal{K}_i^{(0)}$, where the superscript denotes the splitting way under Hamiltonian (7) and the subscript denotes the different Krylov subspaces; see Fig. 2(a). There are two largest Krylov subspaces with the same dimension, labeled as $\mathcal{K}_{\text{cdw1}}^{(0)}$ and $\mathcal{K}_{\text{cdw2}}^{(0)}$, which contain, respectively, the charge-density-wave states $|\text{CDW1}\rangle = |1010 \dots 10\rangle$ and $|\text{CDW2}\rangle = |0101 \dots 01\rangle$, and they lie in the symmetry spaces $\mathcal{S}_{m_{\text{cdw1}}}^{(0)}$ and $\mathcal{S}_{m_{\text{cdw2}}}^{(0)}$ with $e_{m_{\text{cdw1}}} = -N(N-1)$ and $e_{m_{\text{cdw2}}} = -N^2$. In the inset of Fig. 2(a), we show $\max[\mathcal{D}_{\mathcal{K}^{(0)}}]/\mathcal{D}$, the dimension ratio between the largest Krylov subspace and the half-filling sector, as a function of the system size. This ratio decays exponentially with L and tends to 0 in the thermodynamic limit, implying a strong HSF in the half-filling sector.

For the signature of this HSF at large values of g , we study EE $S(kT)$ as a function of the driving cycle k , starting from Fock states. In Fig. 2(b), we show the average EE $S(kT)$ in all Fock states (34 in total) in $\mathcal{K}_{\text{cdw1}}^{(0)}$ at different values of g . The other parameters are $\omega = g/2$ and $u = 1$. For small values of g , $S(kT)$ saturates to the Page value S_p in the half-filling sector but not $S_p[\mathcal{S}_{m_{\text{cdw1}}}^{(0)}]$ in $\mathcal{S}_{m_{\text{cdw1}}}^{(0)}$, indicating that the system is not fragmented and thermalizes within the half-filling sector. For a larger g , $S(kT)$ saturates to $S_p[\mathcal{K}_{\text{cdw1}}^{(0)}]$, which is consistent with the HSF under Hamiltonian (7). The results in $\mathcal{K}_{\text{cdw2}}^{(0)}$, which are qualitatively the same, are not shown here.

This HSF at large tilting strength is further signatored by the value of the saturated density profile. In Fig. 2(d), we plot the saturated density profile \bar{n}_j at different values of g . The parameters and initial conditions are the same as that in Fig. 2(b). \bar{n}_j is obtained by averaging $n_j(kT)$ over the driving

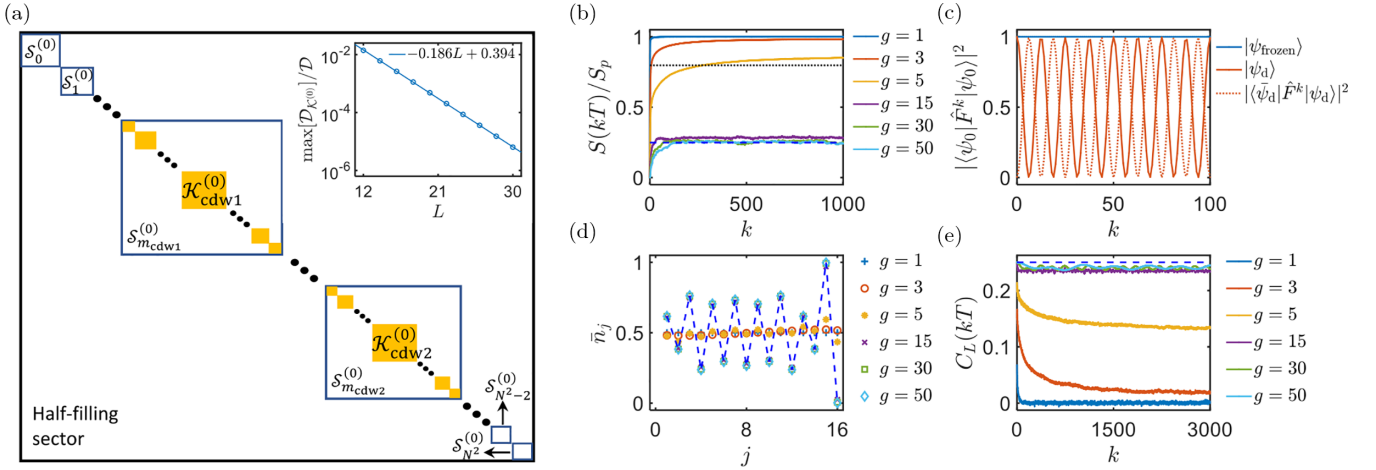


FIG. 2. Schematics of the HSF in the half-filling sector and the signatures of HSF at nonresonance frequencies and large values of g . (a) Schematic of the HSF under the action of Hamiltonian (7). Symmetry spaces $\mathcal{S}_m^{(0)}$ are denoted by blue squares. The Krylov subspaces $\mathcal{K}_i^{(0)}$ are denoted by the filled orange squares. The two largest Krylov subspaces $\mathcal{K}_{cdw1}^{(0)}$ and $\mathcal{K}_{cdw2}^{(0)}$ lie in the symmetry spaces $\mathcal{S}_{m_{cdw1}}^{(0)}$ and $\mathcal{S}_{m_{cdw2}}^{(0)}$, respectively. Inset: semilog plot of the dimension ratio between the largest Krylov subspace and the half-filling sector, as a function of the system size. The blue circles denote the numerical data, and the blue line denotes the fitting function. (b) Averaged and normalized EE $S(kT)/S_p$ vs the driving cycle k at different values of g and for initial states in $\mathcal{K}_{cdw1}^{(0)}$. Black dotted and blue dashed lines denote $S_p[\mathcal{S}_{m_{cdw1}}^{(0)}]/S_p$ and $S_p[\mathcal{K}_{cdw1}^{(0)}]/S_p$, respectively. (c) At $g = 50$, the fidelity dynamics from the frozen state $|\psi_{\text{frozen}}\rangle = |1111111010000000\rangle$ (blue line) and the domain state $|\psi_d\rangle = |000000011111111\rangle$ (red line). The red dotted line shows the amplitude of state transfer from $|\psi_d\rangle$ to $|\tilde{\psi}_d\rangle = |000000010111111\rangle$. (d) \bar{n}_j at different values of g for the initial states in $\mathcal{K}_{cdw1}^{(0)}$. The blue dashed line denotes $n_j[\mathcal{K}_{cdw1}^{(0)}]$. (e) $C_L(kT)$ vs the driving cycle k for different values of g , starting from a random infinite-temperature state. The blue dashed line denotes the lower bound $C_L^{(0)}$ predicted by the HSF due to Hamiltonian (7). In (b), (d), and (e), the data with $g = 15, 30$, and 50 almost collapse with each other. The other parameters in (b)–(e) are $u = 1$, $\omega = g/2$, and $L = 16$. The energies are scaled in units of J .

cycles $k \in [900, 1000]$ and over all initial states. For comparison, we also plot the density profile $n_j[\mathcal{K}_{cdw1}^{(0)}]$, calculated through Eq. (13). For small values of g , \bar{n}_j concentrate on 0.5 for all lattice sites, which is the result of thermalization within the half-filling sector of a driven system. For a larger g , the density profile is consistent with $n_j[\mathcal{K}_{cdw1}^{(0)}]$, again displaying a signature of the HSF under Hamiltonian (7). The results in $\mathcal{K}_{cdw2}^{(0)}$ are qualitatively the same, which are not shown here.

Apart from the large Krylov subspaces, there are numerous frozen states and small Krylov subspaces. The frozen states correspond to the Fock states, which are zero-energy eigenstates of Hamiltonian (7). Any Fock state is frozen under the action of Hamiltonian (7) if it lacks both the configurations “...0011...” and “...0101...”, where the sequences 011 and 101 are away from the left particles by at least one site. In Fig. 2(c), we plot the evolution of the fidelity $|\langle \psi_0 | \hat{F}^k | \psi_0 \rangle|^2$ from a frozen state $|\psi_0\rangle = |\psi_{\text{frozen}}\rangle$ at $g = 50$, $\omega = g/2$, and $u = 1$. The fidelity remains near 1 for all the time considered, evidencing that the state stays closed to the initial state. Furthermore, we study the dynamics in a Krylov subspace with two elements, which contains a state $|\psi_d\rangle$ and its partner $|\tilde{\psi}_d\rangle = \hat{H}_{\omega_q}^{\text{eff}} |\psi_d\rangle$. In Fig. 2(c), we plot the fidelity dynamics with the initial state $|\psi_0\rangle = |\psi_d\rangle$. The fidelity oscillates periodically, and the state transfers almost perfectly between $|\psi_d\rangle$ and $|\tilde{\psi}_d\rangle$; see the red solid and dotted lines in Fig. 2(c). The oscillation period in units of the driving period is 12.5, which is consistent with the value $\omega/2J$ predicted by projecting the effective Hamiltonian (7) into the two-dimensional Krylov subspace.

Finally, we study the autocorrelation function $C_{j=L}(kT)$ starting from a random infinite-temperature state. The results make little difference for different infinite-temperature states. The lower bound of the autocorrelation function for $j = L$ is $C_L^{(0)} = 0.25$. This value is exact and obtained by the following analysis. The particle number at site L is frozen under the action of Hamiltonian (7), that is, \hat{n}_L is conserved in each Krylov subspace. So, the trace in Eq. (12) equals $\mathcal{D}_{\mathcal{K}_i^{(0)}}/2$ or $-\mathcal{D}_{\mathcal{K}_i^{(0)}}/2$ for an arbitrary $\mathcal{K}_i^{(0)}$, and it leads to $C_L^{(0)} = 0.25$. In Fig. 2(e), we plot the evolution of $C_L(kT)$ for different values of g . The other parameters are $\omega = g/2$ and $u = 1$. For small values of g , $C_L(kT)$ quickly decays to zero, which is the result of thermalization in the half-filling sector. As g increases, $C_L(kT)$ saturates to finite values and tends to the bound $C_L^{(0)}$. All these results are consistent with the fact that the half-filling sector is split strongly according to the Hamiltonian (7) for large values of g .

We note that when the driving is absent with $u = 0$, the effective Hamiltonian at large values of g is the same as the Hamiltonian (7). Thus, for a long range of time, the Hilbert space is split in the same way as that studied in this section; see Appendix C.

B. Algebraic strong Hilbert space fragmentation at the resonance frequency $\omega_1^r = g$

When the driving frequency $\omega = \omega_1^r$, the tunneling processes projected by $\hat{P}_{j-1,j+2}^{(0)}$ and $\hat{P}_{j-1,j+2}^{(g)}$ are allowed, while the one projected by $\hat{P}_{j-1,j+2}^{(2g)}$ vanishes. The effective Floquet

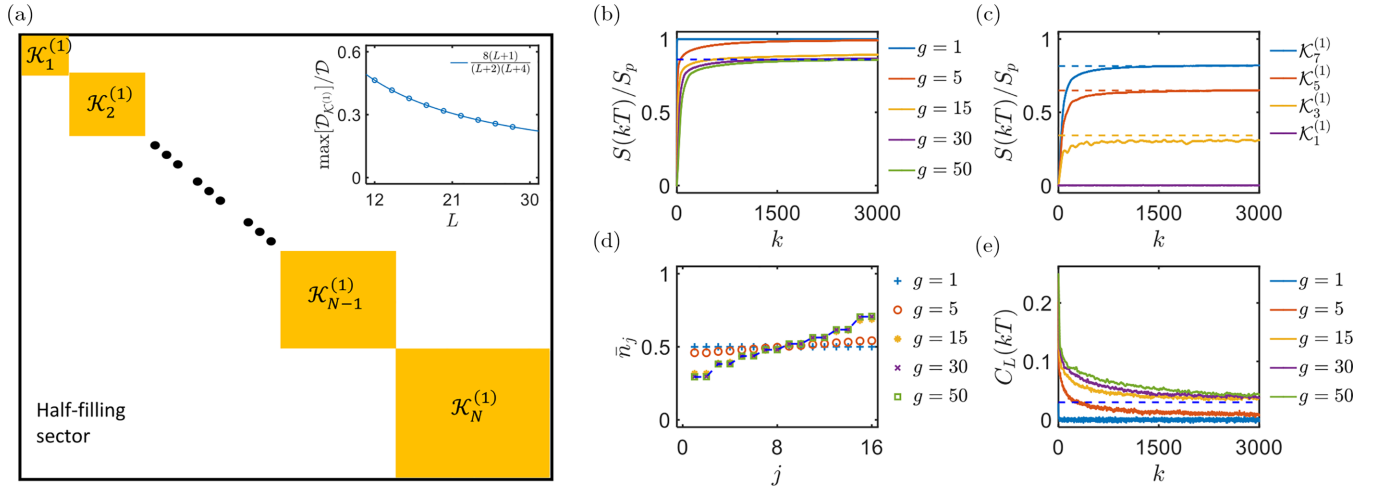


FIG. 3. Schematics of the HSF in the half-filling sector and the signatures of HSF at $\omega = \omega_r^i$ and large values of g . (a) Schematic of the HSF under the action of the Hamiltonian (8). The Krylov subspaces $\mathcal{K}_i^{(1)}$ are denoted by the filled orange squares. Inset: the dimension ratio between the largest Krylov subspace and the half-filling sector, as a function of the system size. The blue circles denote the numerical data, and the blue line denotes the fitting function. (b) The averaged and normalized EE $S(kT)/S_p$ vs the driving cycle k at different values of g and for the initial states in $\mathcal{K}_8^{(1)}$. The blue dashed line denotes $S_p[\mathcal{K}_8^{(1)}]/S_p$. (c) Averaged and normalized EE $S(kT)/S_p$ vs k at $g = 50$, for initial states in $\mathcal{K}_7^{(1)}$ (blue line), $\mathcal{K}_5^{(1)}$ (red line), $\mathcal{K}_3^{(1)}$ (yellow line), and $\mathcal{K}_1^{(1)}$ (purple line). The dashed lines with different colors denote $S_p[\mathcal{K}_i^{(1)}]/S_p$ ($i = 7, 5, 3$) of the corresponding Krylov subspaces $\mathcal{K}_i^{(1)}$. For $\mathcal{K}_1^{(1)}$, the Fock state is frozen and $S(kT)$ stays near 0. (d) \bar{n}_j at different values of g for initial states in $\mathcal{K}_8^{(1)}$. The blue dashed line denotes $n_j[\mathcal{K}_8^{(1)}]$. (e) $C_L(kT)$ vs the driving cycle k for different values of g , starting from the same infinite-temperature state in Fig. 2(e). The blue dashed line denotes the lower bound $C_L^{(1)}$ predicted by the HSF due to Hamiltonian (8). In (b), (d), and (e), the numerical data with $g = 15, 30$, and 50 almost collapse with each other. The other parameters in (b)–(e) are $u = 1$, $\omega = g$, and $L = 16$. The energies are scaled in units of J .

Hamiltonian is given by Hamiltonian (8). Compared to Hamiltonian (7), the additional tunneling term in Hamiltonian (8) relaxes some kinetic constraints, thus it changes the structure of the Hilbert space.

Under the action of the Hamiltonian (8), the half-filling sector is split into N Krylov subspaces $\mathcal{K}_i^{(1)}$ ($i = 1, \dots, N$), with the superscript denoting the splitting way under Hamiltonian (8); see Fig. 3(a). Each Krylov subspace $\mathcal{K}_i^{(1)}$ contains the state $|\psi_i\rangle = |(0 \dots 0)^{i-1} (1 \dots 1)^N (0 \dots 0)^{N-i+1}\rangle$ with $(0 \dots 0)^i$ and $(1 \dots 1)^i$ denoting i contiguous empty sites and occupied sites, respectively. The dimension of $\mathcal{K}_i^{(1)}$ increases with i , with $\mathcal{K}_1^{(1)}$ being the minimal subspace with dimension 1 for all system sizes, that is, $|(1 \dots 1)^N (0 \dots 0)^N\rangle$ is a frozen state. In the inset of Fig. 3(a), we plot the dimension ratio $\max[\mathcal{D}_{\mathcal{K}^{(1)}}]/\mathcal{D}$ between the largest Krylov subspace and the half-filling sector as a function of the system size. We numerically find $\max[\mathcal{D}_{\mathcal{K}^{(1)}}]/\mathcal{D} = \frac{8(L+1)}{(L+2)(L+4)}$, with the analytical derivation deserving further study. Unlike the exponential decay in common strong HSF [32–34,37,40], here the ratio tends to zero algebraically with the system size. Thus, we call it algebraic strong HSF. We note that such an algebraic strong HSF has been found in a generalized Fredkin spin chain with long-range interaction [39].

The fact that the half-filling sector is split into N Krylov subspaces may suggest that the Hamiltonian (8) has some obvious local symmetry and the Krylov subspaces can be labeled by the corresponding quantum number. However, we do not find any obvious conserved quantities here (except the total particle number). In fact, in Hamiltonian (8), the first term conserves the on-site energy, while the second term changes

the eigenvalues of \hat{H}_{on} by $\pm g$, which can be viewed as the system emits or absorbs a “photon” with frequency g . The total energy $\hat{H}_{\text{on}} + \hat{n}_{p_1}g = (\hat{\epsilon} + \hat{n}_{p_1})g$ is conserved, where \hat{n}_{p_1} is the “photon” number. Because \hat{n}_{p_1} cannot be expressed as fermion operators, we cannot deduce any conserved quantity about the fermions from this energy conservation law. It can be contrasted with the case in Sec. III A, where the “photon” number is fixed and thus $\hat{\epsilon}$ is conserved. It will also contrast with the case in Sec. III C, where the “photon” frequency is $2g$ and thus the parity of $\hat{\epsilon}$ is conserved.

For the signature of this HSF, we calculate the EE dynamics, the saturated density profile, and the density autocorrelation function dynamics by the exact time evolution at $\omega = g$ and $u = 1$. In Fig. 3(b), we plot $S(kT)/S_p$ versus the driving cycle k at different values of g for initial states in the largest Krylov subspace $\mathcal{K}_8^{(1)}$. The EE are averaged over 50 random initial Fock states in $\mathcal{K}_8^{(1)}$. For small values of g , $S(kT)$ rapidly saturates to S_p . As g increases, $S(kT)$ begins to saturate to smaller values and reaches $S_p[\mathcal{K}_8^{(1)}]$ over a long period of time. At a large value of g , the EE for the Fock states in the other Krylov subspaces also saturates to the Page value of the corresponding Krylov subspaces. In Fig. 3(c), we plot $S(kT)/S_p$ at $g = 50$ in Krylov subspaces $\mathcal{K}_7^{(1)}$, $\mathcal{K}_5^{(1)}$, $\mathcal{K}_3^{(1)}$, and $\mathcal{K}_1^{(1)}$. For $\mathcal{K}_{7,5,3}^{(1)}$, the EEs are averaged over 50 initial random Fock states, and they saturate to values $S_p[\mathcal{K}_{7,5,3}^{(1)}]$, respectively. For $\mathcal{K}_1^{(1)}$, the EE remains close to 0, which is consistent with the prediction of the frozen state.

Figure 3(d) shows the saturated density profile \bar{n}_j at different values of g , for the same initial states as that in Fig. 3(b).

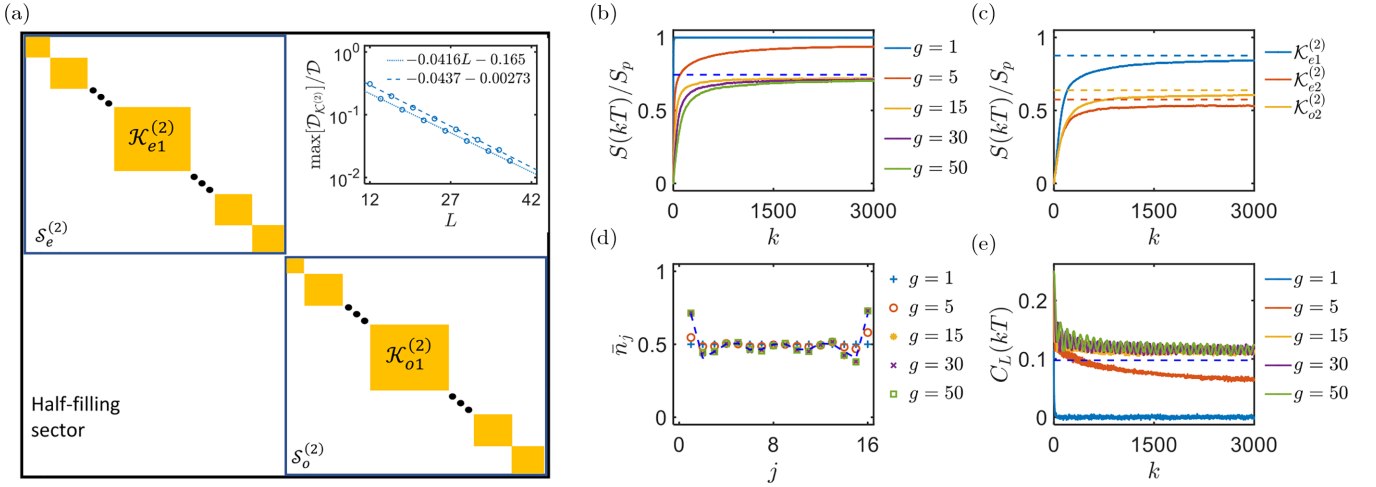


FIG. 4. Schematics of the HSF in the half-filling sector and the signatures of HSF at $\omega = \omega_2^r$ and large values of g . (a) Schematic of the HSF under the action of the Hamiltonian (9). The even- and odd-parity symmetry spaces $S_e^{(2)}$ and $S_o^{(2)}$ are denoted by the empty blue squares. The Krylov subspaces $\mathcal{K}_i^{(2)}$ are denoted by the filled orange squares. Inset: semilog plot of the dimension ratio between the largest Krylov subspace and the half-filling sector, as a function of the system size. The blue circles denote the numerical data. The blue dashed and dotted lines denote the fitting functions for quadruple and nonquadruple lattice sites, respectively. (b) Averaged and normalized EE $S(kT)/S_p$ vs the driving cycle k at different values of g and for the initial states in $\mathcal{K}_{o1}^{(2)}$. The blue dashed line denotes $S_p[\mathcal{K}_{o1}^{(2)}]/S_p$. (c) Averaged and normalized EE $S(kT)/S_p$ vs k at $g = 50$, for initial states in $\mathcal{K}_{e1}^{(2)}$ (blue line), $\mathcal{K}_{e2}^{(2)}$ (red line), and $\mathcal{K}_{o2}^{(2)}$ (yellow line). The dashed lines with different colors denote the normalized Page value of EE of the corresponding Krylov subspaces. (d) \bar{n}_j at different values of g for the initial states in $\mathcal{K}_{o1}^{(2)}$. The blue dashed line denotes $n_j[\mathcal{K}_{o1}^{(2)}]$. (e) $C_L(kT)$ vs k for different values of g , starting from the same infinite-temperature state in Fig. 2(e). The blue dashed line denotes the lower bound $C_L^{(2)}$ predicted by the HSF due to the Hamiltonian (9). In (b), (d), and (e), the numerical data with $g = 15, 30$, and 50 almost collapse with each other. The other parameters in (b)–(e) are $u = 1$, $\omega = 2g$, and $L = 16$. Energies are scaled in units of J .

It is obtained by averaging $n_j(kT)$ over the driving cycles $k \in [2900, 3000]$ and over all the initial states. For small values of g , \bar{n}_j shows a uniform profile around 0.5. For large values of g , \bar{n}_j is consistent with $n_j[\mathcal{K}_s^{(1)}]$.

Finally, Fig. 3(e) shows the evolution of $C_L(kT)$ for different values of g , starting from the same infinite-temperature state as that in Fig. 2(e). The results make little difference for different infinite-temperature states. For small g , $C_L(kT)$ quickly decays to zero. For a large g , $C_L(kT)$ saturates to $C_L^{(1)}$ predicted by the present HSF. All these results are consistent with the fact that the half-filling sector is split strongly according to the Hamiltonian (8) at $\omega = \omega_1^r$ in the large tilt limit.

C. Exponential strong Hilbert space fragmentation at the resonance frequency $\omega_2^r = 2g$

When the driving frequency $\omega = \omega_2^r$, the tunneling processes projected by $\hat{P}^{(0)}$ and $\hat{P}^{(2g)}$ are resonant. The tunneling process projected by $\hat{P}^{(g)}$ is off-resonant and can be neglected. The effective Floquet Hamiltonian is given by Hamiltonian (9), which conserves the parity $\hat{P}_e = (-1)^{\hat{e}}$ of \hat{e} . As mentioned before, the conservation of \hat{P}_e can be understood as a result of the conservation of energy $\hat{H}_{\text{on}} + 2\hat{n}_{p_2}g = (\hat{e} + 2\hat{n}_{p_2})g$, where \hat{n}_{p_2} is the number of ‘‘photons’’ with frequency $2g$.

The action of Hamiltonian (9) splits the half-filling sector into Krylov subspaces $\mathcal{K}_i^{(2)}$ beyond the conservation of \hat{P}_e , where the superscript of $\mathcal{K}_i^{(2)}$ denotes the splitting way under Hamiltonian (9) and the subscript denotes the

different Krylov subspaces; see Fig. 4(a). It should be noted that the two allowed processes are related by a spatial-reflection transformation, i.e., $\hat{R}[\hat{P}_{j-1,j+2}^{(0)}(\hat{c}_j^\dagger\hat{c}_{j+1} + \text{H.c.})]\hat{R}^{-1} = \hat{P}_{L-j-1,L-j+2}^{(2g)}(\hat{c}_{L-j+1}^\dagger\hat{c}_{L-j} + \text{H.c.})$, where the spatial-reflection operator \hat{R} is defined by $\hat{R}|n_0n_1 \cdots n_{L-2}n_{L-1}\rangle = |n_{L-1}n_{L-2} \cdots n_1n_0\rangle$. This leads to an odd-even effect of the particle number on the splitting of the Hilbert space (see Appendix D for details). When the particle number N is odd, the Krylov subspaces in the even- and odd-parity symmetry space $S_e^{(2)}$ and $S_o^{(2)}$ are in one-to-one correspondence through the spatial-reflection transformation. Thus, there are two largest Krylov subspaces with the same dimension, labeled as $\mathcal{K}_{e1}^{(2)}$ and $\mathcal{K}_{o1}^{(2)}$, which are in $S_e^{(2)}$ and $S_o^{(2)}$, respectively. When N is even, there exist reflection-invariant Krylov subspaces, and the largest Krylov subspace $\mathcal{K}_{e1}^{(2)}$ lies in $S_e^{(2)}$. So, the scaling of the dimension ratio between the largest Krylov subspace and the half-filling sector is different for quadruple and nonquadruple lattice sites, and we need two functions to fit them. In the inset of Fig. 4(a), we plot this ratio as a function of the system size. It shows exponential decay with the system size and vanishes in the thermodynamic limit, which implies strong HSF with respect to the half-filling sector.

For the signature of this HSF, we calculate the EE dynamics, the saturated density profile, and the density autocorrelation function dynamics by the exact time evolution at $\omega = 2g$ and $u = 1$. In Fig. 4(b), we plot $S(kT)/S_p$ versus the driving cycle k at different values of g for the initial states in the largest Krylov subspace $\mathcal{K}_{o1}^{(2)}$ within the odd-parity space. The EEs are averaged over 50 initial random Fock states in

$\mathcal{K}_{o1}^{(2)}$. For small values of g , $S(kT)$ rapidly saturates to S_p . As g increases, $S(kT)$ starts to saturate to smaller values and reaches $S_p[\mathcal{K}_{o1}^{(2)}]$ for a long range of time. At a large value of g , the EE for Fock states in other Krylov subspaces also saturates to the Page value of the corresponding Krylov subspace. In Fig. 4(c), we plot $S(kT)/S_p$ at $g = 50$ for initial states in the largest and second largest Krylov subspace $\mathcal{K}_{e1}^{(2)}$ and $\mathcal{K}_{e2}^{(2)}$ within the even-parity space, and the second largest Krylov subspace $\mathcal{K}_{o2}^{(2)}$ within the odd-parity space. For all the Krylov subspaces, the EE are calculated by averaging 50 initial random Fock states, and they saturate to the Page values of the corresponding Krylov subspaces.

Figure 4(d) shows the saturated density profile \bar{n}_j at different values of g for the same initial states as those in Fig. 4(b). It is obtained by averaging $n_j(kT)$ over the driving cycles $k \in [2900, 3000]$ and over all the initial states. For small values of g , \bar{n}_j shows a uniform profile around 0.5. For large values of g , \bar{n}_j is consistent with $n_j[\mathcal{K}_{o1}^{(2)}]$.

Finally, Fig. 4(e) shows the evolution of $C_L(kT)$ for different values of g , starting from the same infinite-temperature state as that in Fig. 2(e). The results make little difference for different infinite-temperature states. For small g , $C_L(kT)$ quickly decays to zero. For a large g , $C_L(kT)$ saturates to $C_L^{(2)}$ predicted by the present strong HSF. All these results are consistent with the fact that the half-filling sector is split strongly according to Hamiltonian (9) at $\omega = \omega_2^r$ in the large tilt limit.

D. Tuning the Hilbert space fragmentation by controlling the driving frequency

Now, we have established that the Hilbert space will split in three different ways at different driving frequencies in the large tilting limit. To clearly show the tuning of the HSF by controlling the driving frequency, we study the evolution of $S(kT)$ from one Fock state $|\psi_0\rangle$ and of $C_L(kT)$ from the infinite-temperature state in Figs. 2(e), 3(e), and 4(e).

In Fig. 5(a), we plot the growth of the normalized EE from the initial state $|\psi_0\rangle = |1010011001101001\rangle$, for $\omega = g/2$, $g/1.5$, $2g$, and g , $g = 50$, and $u = 1$. The initial state is chosen in some random way, but requiring that the Page values of EE $S_p[\mathcal{K}_{\psi_0}^{(0)}]$, $S_p[\mathcal{K}_{\psi_0}^{(1)}]$, and $S_p[\mathcal{K}_{\psi_0}^{(2)}]$ are sufficiently different for better illustration, where $\mathcal{K}_{\psi_0}^{(0)}$, $\mathcal{K}_{\psi_0}^{(1)}$, and $\mathcal{K}_{\psi_0}^{(2)}$ are the Krylov subspaces to which $|\psi_0\rangle$ belongs. For $\omega = g$ and $2g$, the EE saturates to $S_p[\mathcal{K}_{\psi_0}^{(1)}]$ and $S_p[\mathcal{K}_{\psi_0}^{(2)}]$, respectively. For the other two frequencies, the EE saturates to $S_p[\mathcal{K}_{\psi_0}^{(0)}]$. In Fig. 5(b), we plot the normalized saturated EE \bar{S}/S_p versus g/ω for $|\psi_0\rangle$ at $g = 50$ and $u = 1$. \bar{S} is calculated by averaging $S(kT)$ over the driving cycles $k \in [1900, 2000]$. We see two clear peaks at $\omega = \omega_1^r$ and ω_2^r , where the saturated EE is consistent with $S_p[\mathcal{K}_{\psi_0}^{(1)}]$ and $S_p[\mathcal{K}_{\psi_0}^{(2)}]$, respectively. At other frequencies, the saturated EE is consistent with $S_p[\mathcal{K}_{\psi_0}^{(0)}]$.

In Fig. 5(c), we plot the saturated density autocorrelation function \bar{C}_L versus g/ω at $g = 50$ and $u = 1$. \bar{C}_L is obtained by averaging $C_L(kT)$ over the driving cycles $k \in [5900, 6000]$. It shows two dips at $\omega = \omega_1^r$ and ω_2^r , which is consistent with the predicted value $C_L^{(1)}$ and $C_L^{(2)}$, respectively. For other values of ω , \bar{C}_L is consistent with $C_L^{(0)}$.

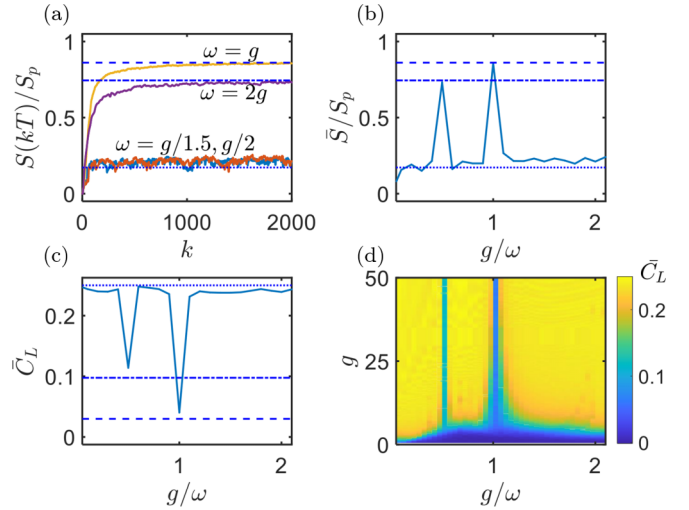


FIG. 5. (a) $S(kT)/S_p$ vs the driving cycle k for different driving frequencies $\omega = g/2$ (blue line), $g/1.5$ (red line), and $2g$ (purple line). The initial state is $|\psi_0\rangle = |1010011001101001\rangle$. (b) \bar{S}/S_p vs g/ω , with the same initial state in (a). In (a) and (b), the blue dotted, dashed, and dot-dashed lines denote the three normalized Page values $S_p[\mathcal{K}_{\psi_0}^{(0)}]/S_p$, $S_p[\mathcal{K}_{\psi_0}^{(1)}]/S_p$, and $S_p[\mathcal{K}_{\psi_0}^{(2)}]/S_p$, respectively. (c) \bar{C}_L vs g/ω , starting from the same infinite-temperature state in Figs. 2(e), 3, and 4(e). The blue dotted, dashed, and dot-dashed lines denote $C_L^{(0)}$, $C_L^{(1)}$, and $C_L^{(2)}$, respectively. In (a)–(c), the other parameters are $u = 1$, $g = 50$, and $L = 16$. (d) \bar{C}_L as a function of $(g, g/\omega)$ at $u = 1$ and system size $L = 12$. In all plots, the energies are scaled in units of J .

In Fig. 5(d), we plot a phase diagram on the parameter plane $(g, g/\omega)$ at $u = 1$ and $L = 12$, which shows the thermal and three kinds of HSF features of \bar{C}_L . For $\omega = \omega_1^r$ and ω_2^r , \bar{C}_L shows a crossover from 0 to $C_L^{(1)}$ and $C_L^{(2)}$, respectively, as g increases, while for other values of ω , it shows a crossover to $C_L^{(0)}$.

We note that, similar to Ref. [46], the HSF studied in this work is a prethermal phenomenon and it survives over a finite long period of time. In the long-time limit, the system will thermalize due to the higher-order corrections. In Appendix E, we study the thermalization time as a function of the tilting strength. The thermalization time increases exponentially with g , indicating that the HSF signature can be found for a long period of time.

The above features show that one can tune the HSF by controlling the driving frequency when the tilting strength is sufficiently strong.

IV. SUMMARY

In conclusion, we have proposed a scheme to tune the HSF within the half-filling sector, through Floquet engineering of constrained tunnelings in a strongly tilted lattice. Through the time-dependent perturbation theory in Floquet systems, we analytically derive two resonance frequencies, at which some particular tunneling processes are resonant. At the nonresonance frequencies, the system is kinetically constrained and stays in a strong fragmented phase, which is the same as that in the case without driving. At the

two resonance frequencies, we engineer two effective Hamiltonians that release some kinetic constraints in different ways. The releasing of the kinetic constraints changes the structure of the Hilbert space and leads to another two kinds of strong Hilbert space fragmentation. The three kinds of Hilbert space fragmentation are supported by the EE, the saturated density profile, and the density autocorrelation functions from the exact time evolution. Our results provide an efficient way to tune the Hilbert space fragmentation by controlling the driving frequency of interacting particles tunneling in tilted lattice systems. The possibility to control the hopping channels by tuning the resonance between the driving and the system provides a new opportunity to study the relation between kinetic constraints and other ergodicity breaking phenomena, such as quantum many-body scars [29,63].

ACKNOWLEDGMENTS

This study is supported by the National Natural Science Foundation of China (Grants No. 12025509 and No. 12305048), Shenzhen Fundamental Research Project (Grants No. JCYJ20230808105009018), and the National Key Research and Development Program of China (Grant No. 2022YFA1404104). Y.K. is supported by the National Natural Science Foundation of China (Grant No. 12275365) and the Natural Science Foundation of Guangdong (Grant No. 2023A1515012099).

APPENDIX A: PROPOSAL FOR THE COSINE DRIVING PROTOCOL

We discuss a scheme to realize our model $\hat{H}(t) = \hat{H}_J(t) + \hat{H}_U + \hat{H}_g$ in the Rydberg atom platform, where $\hat{H}_J(t) = J[1 + u \cos(\omega t)] \sum_j (\hat{c}_j^\dagger \hat{c}_{j+1} + \text{H.c.})$, $\hat{H}_U = U \sum_j \hat{n}_j \hat{n}_{j+1}$, and $\hat{H}_g = -g \sum_j j \hat{n}_j$.

We consider a one-dimensional chain of L Rydberg atoms, with lattice constant a and each trapped in optical tweezers [64–68]. Two Rydberg states are chosen to simulate the empty state and the fermion occupied state with $|0\rangle = |nS\rangle$ and $|1\rangle = |n'P\rangle$, where $|nS\rangle$ and $|n'P\rangle$ are the two Rydberg states with principal quantum numbers n and n' ($n \simeq n'$) and angular momentum S and P , respectively (we note that n labels the principal quantum number in this Appendix and the fermions number in the main text). The Rydberg atom chain is subjected to a gradient magnetic field, which causes an effective Zeeman splitting M_j between the two Rydberg states with $M_j - M_{j+1} = \tilde{g}$, as described by the Hamiltonian $\hat{H}_g = -\tilde{g} \sum_j j(|n'P\rangle\langle n'P|)_j$.

Utilizing the gradient magnetic field and a laser-assisted dipole-dipole (DD) interaction between Rydberg atoms [69],

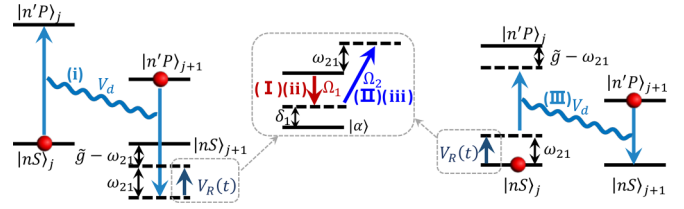


FIG. 6. The two Raman-assisted three-order transition processes coupling $|nS\rangle_j |n'P\rangle_{j+1}$ to $|n'P\rangle_j |nS\rangle_{j+1}$. The left energy level scheme denotes the three-order transition process $|nS\rangle_j |n'P\rangle_{j+1} \rightarrow |n'P\rangle_j |nS\rangle_{j+1} \rightarrow |n'P\rangle_j |\alpha\rangle_{j+1} \rightarrow |n'P\rangle_j |nS\rangle_{j+1}$, in which the first process (i) is the bare exchange interaction and the second (ii) and third processes (iii) induce a two-photon detuning $\omega_{21} = \omega_{R_2} - \omega_{R_1}$. The right energy level scheme denotes the three-order transition process $|nS\rangle_j |n'P\rangle_{j+1} \rightarrow |\alpha\rangle_j |n'P\rangle_{j+1} \rightarrow |nS\rangle_j |n'P\rangle_{j+1} \rightarrow |n'P\rangle_j |nS\rangle_{j+1}$, in which the first and second processes (I) and (II) induce the two-photon detuning ω_{21} and the third process (III) is the exchange interaction.

we can realize the term $\hat{H}_g + \hat{H}_J(t)$. For two atoms in different Rydberg states, there is a DD interaction between them, which scales as $1/R^3$, with R being the distance between the two atoms [66,68]. For a sufficiently large lattice constant a , one can only consider the nearest-neighboring DD interaction. The direct DD interaction between the site j and $j + 1$ exchanges the Rydberg states at the two sites and reads $V_d[(|nS\rangle\langle n'P|)_j (|n'P\rangle\langle nS|)_{j+1} + \text{H.c.}]$, with $V_d = C_3/a^3$ and $C_3 \sim n^4$ being the DD interaction coefficient [66]. It simulates the tunneling term in our model. To make the tunneling strength periodically vary in time, we propose a Raman coupling scheme, which contains two Raman lasers coupling the state $|nS\rangle$ to a low-lying state $|\alpha\rangle$, as described by

$$V_R(t) = \sum_j \{ [\Omega_1 \cos(\omega_{R_1} t) + \Omega_2 \cos(\omega_{R_2} t)] (|nS\rangle\langle \alpha|)_j + \text{H.c.} \}. \quad (\text{A1})$$

Here, $\Omega_{1,2}$ are the Rabi frequencies, and ω_{R_1, R_2} are the frequencies of the two Raman lasers. We suppose that the tilting strength \tilde{g} is much larger than V_d , and the bare exchange process is suppressed due to this energy offset. In the same spirit of Ref. [69], we utilize the two-photon Raman process to compensate part of the energy offset with $\tilde{g} - (\omega_{R_2} - \omega_{R_1}) = g$ and recover the exchange coupling.

There are two intermediate states $|n'P\rangle_j |\alpha\rangle_{j+1}$ and $|\alpha\rangle_j |n'P\rangle_{j+1}$ that help the coupling between $|nS\rangle_j |n'P\rangle_{j+1}$ and $|n'P\rangle_j |nS\rangle_{j+1}$, with the energy compensation happening at site $j + 1$ and j , respectively; see Fig. 6. Labeling $|a\rangle_j = |nS\rangle_j |n'P\rangle_{j+1}$, $|b\rangle_j = |\alpha\rangle_j |n'P\rangle_{j+1}$, $|c\rangle_j = |n'P\rangle_j |\alpha\rangle_{j+1}$, and $|d\rangle_j = |n'P\rangle_j |nS\rangle_{j+1}$, the laser-assisted DD interaction in the four-level system under a rotating-wave approximation reads

$$\hat{H}^{\text{LDD}}(j, t) = \begin{pmatrix} E_a & \frac{\Omega_1}{2} e^{-i\omega_{R_1} t} + \frac{\Omega_2}{2} e^{-i\omega_{R_2} t} & 0 & V_d \\ \frac{\Omega_1^*}{2} e^{i\omega_{R_1} t} + \frac{\Omega_2^*}{2} e^{i\omega_{R_2} t} & E_b & 0 & 0 \\ 0 & 0 & E_c & \frac{\Omega_1^*}{2} e^{i\omega_{R_1} t} + \frac{\Omega_2^*}{2} e^{i\omega_{R_2} t} \\ V_d & 0 & \frac{\Omega_1}{2} e^{-i\omega_{R_1} t} + \frac{\Omega_2}{2} e^{-i\omega_{R_2} t} & E_d \end{pmatrix}, \quad (\text{A2})$$

where $E_d - E_a = \tilde{g}$, $E_a - E_b = E_d - E_c = \Delta$, and Δ is the energy difference between $|nS\rangle$ and $|\alpha\rangle$. Transforming to the interaction picture, the Hamiltonian reads

$$\hat{H}_1^{\text{LDD}}(j, t) = \begin{pmatrix} 0 & \frac{\Omega_1}{2} e^{i\delta_1 t} + \frac{\Omega_2}{2} e^{i\delta_2 t} & 0 & V_d e^{-i\tilde{g}t} \\ \frac{\Omega_1^*}{2} e^{-i\delta_1 t} + \frac{\Omega_2^*}{2} e^{-i\delta_2 t} & 0 & 0 & 0 \\ 0 & 0 & 0 & \frac{\Omega_1^*}{2} e^{-i\delta_1 t} + \frac{\Omega_2^*}{2} e^{-i\delta_2 t} \\ V_d e^{i\tilde{g}t} & 0 & \frac{\Omega_1}{2} e^{i\delta_1 t} + \frac{\Omega_2}{2} e^{i\delta_2 t} & 0 \end{pmatrix}, \quad (\text{A3})$$

with $\delta_1 = \Delta - \omega_{R_1}$ and $\delta_2 = \Delta - \omega_{R_2}$ being the single-photon detunings. In the interaction picture, the evolution operator can be expanded in the Dyson series as

$$\begin{aligned} \hat{U}_1(j, t) = & 1 - i \int_0^t \hat{H}_1^{\text{LDD}}(j, t_1) dt_1 + (-i)^2 \int_0^t \hat{H}_1^{\text{LDD}}(j, t_1) \int_0^{t_1} \hat{H}_1^{\text{LDD}}(j, t_2) dt_2 dt_1 \\ & + (-i)^3 \int_0^t \hat{H}_1^{\text{LDD}}(j, t_1) \int_0^{t_1} \hat{H}_1^{\text{LDD}}(j, t_2) \int_0^{t_2} \hat{H}_1^{\text{LDD}}(j, t_3) dt_3 dt_2 dt_1 + \dots \end{aligned} \quad (\text{A4})$$

Suppose \tilde{g} , $|\delta_1|$, $|\delta_2|$, $|\tilde{g} \pm \delta_1|$, $|\tilde{g} \pm \delta_2|$, $|\delta_1 - \delta_2| \gg V_d$, $|\Omega_1|$, $|\Omega_2|$, and $\tilde{g} \sim \omega_{R_2} - \omega_{R_1}$. The first- and second-order processes are nonresonant. In the third-order processes, the couplings between $\{|a\rangle_j, |d\rangle_j\}$ and $\{|b\rangle_j, |c\rangle_j\}$ are nonresonant, and there are near-resonant couplings between $|a\rangle_j |b\rangle_j$ and $|d\rangle_j |c\rangle_j$. Thus, the evolution operator in the interaction picture is block-diagonalized. According to the near-resonant processes in Fig. 6, we can calculate the element matrix

$$U_1^{(ad)} = {}_j \langle d | \hat{U}_1(j, t) | a \rangle_j = J_{\text{eff}} \frac{e^{-i(\omega_{21} - \tilde{g})t} - 1}{\omega_{21} - \tilde{g}},$$

where $\omega_{21} = \omega_{R_2} - \omega_{R_1}$, and

$$J_{\text{eff}} = \frac{V_d \Omega_1^* \Omega_2}{4} \left[\frac{1}{\delta_1 \omega_{21}} + \frac{1}{\tilde{g}(\tilde{g} - \delta_1)} \right]. \quad (\text{A5})$$

The evolution operator in the bases $\{|a\rangle_j, |d\rangle_j\}$ up to a third-order Dyson expansion then reads

$$\hat{U}_1^{(ad)}(j, t) \approx 1 + [U_1^{(ad)}(|d\rangle\langle a|_j - \text{H.c.})]. \quad (\text{A6})$$

Transforming to the Schrödinger picture, we can obtain the Hamiltonian

$$\begin{aligned} \hat{H}^{(ad)}(j, t) = & \hat{H}_0(j) + i e^{-i\hat{H}_0(j)t} \frac{\partial \hat{U}_1^{(ad)}}{\partial t} \hat{U}_1^{(ad)\dagger} e^{i\hat{H}_0(j)t} \\ = & \hat{H}_0(j) + J_{\text{eff}} e^{-i(\omega_{21} - \tilde{g} + E_d - E_a)t} (|d\rangle\langle a|_j + \text{H.c.}), \end{aligned} \quad (\text{A7})$$

where $\hat{H}_0(j) = E_a(|a\rangle\langle a|_j + |d\rangle\langle d|_j)$. Finally, we perform a rotating transformation and obtain the effective Hamiltonian

$$\begin{aligned} \hat{H}_{\text{eff}}^{(ad)}(j) = & \hat{S}(t) \hat{H}^{(ad)}(j, t) \hat{S}^\dagger(t) - i \hat{S}(t) \frac{\partial \hat{S}^\dagger(t)}{\partial t} \\ = & -\frac{\tilde{g} - \omega_{21}}{2} (|a\rangle\langle a|_j + |d\rangle\langle d|_j) \\ & + J_{\text{eff}} (|d\rangle\langle a|_j + \text{H.c.}), \end{aligned} \quad (\text{A8})$$

where

$$\hat{S}(t) = \begin{pmatrix} e^{i(E_a - \frac{\omega_{21} - \tilde{g}}{2})t} & 0 \\ 0 & e^{i(E_d + \frac{\omega_{21} - \tilde{g}}{2})t} \end{pmatrix}. \quad (\text{A9})$$

If we set $\Omega_1 = \Omega_2 = \Omega$, and tune the Rabi frequency as $|\Omega|^2 = |\Omega_0|^2 [1 + u \cos(\omega t)]$, with the cosinoidal drive being realized experimentally [70], the sum of $\hat{H}_{\text{eff}}^{(ad)}(j)$ over j simulates $\hat{H}_g + \hat{H}_J(t)$ with $J = V_d |\Omega_0|^2 [\frac{1}{4\delta_1 \omega_{21}} + \frac{1}{4\tilde{g}(\tilde{g} - \delta_1)}]$ and $g = \tilde{g} - \omega_{21}$.

The van der Waals interaction between Rydberg atoms can be used to simulate \hat{H}_U . The atoms in the same Rydberg states can interact through the van der Waals interaction, which scales as $1/R^6$ [66,68]. If the lattice constant is sufficiently large, one can only consider the nearest-neighboring interaction. The sum of the van der Waals interactions of the two kinds of Rydberg states reads

$$\begin{aligned} \hat{H}_{\text{vdW}} = & \frac{C_6^{(2)} + C_6^{(1)}}{a^6} \sum_{j=0}^{L-2} (|n'P\rangle\langle n'P|_j |n'P\rangle\langle n'P|_{j+1}) \\ & + \frac{C_6^{(1)}}{a^6} [(|n'P\rangle\langle n'P|)_0 + (|n'P\rangle\langle n'P|)_{L-1}], \end{aligned} \quad (\text{A10})$$

where $C_6^{(1)} \sim n^{11}$ and $C_6^{(2)} \sim n'^{11}$ are the van der Waals coefficients of $|nS\rangle$ and $|n'P\rangle$ [66,68], and a constant energy $-LC_6^{(1)}/a^6$ has been dropped. The defect at the boundary sites can be compensated by a light shift. Thus, the van der Waals interaction simulates \hat{H}_U with $U = [C_6^{(2)} + C_6^{(1)}]/a^6$.

APPENDIX B: DERIVATION OF THE EFFECTIVE FLOQUET HAMILTONIAN THROUGH THE TIME-DEPENDENT PERTURBATION APPROACH

In this Appendix, we present the TDPT in Floquet systems [58,59] to derive the effective Floquet Hamiltonian for small tunneling strength. We first introduce the framework of the TDPT in Floquet systems and then apply it to derive the effective Floquet Hamiltonian for our model.

Consider a Hamiltonian $\hat{H}(t) = \hat{H}_s + \lambda \hat{H}_V(t)$, where \hat{H}_s is time-independent and solvable with eigenequation $\hat{H}_s |n\rangle = E_n |n\rangle$, $\hat{H}_V(t)$ is time periodic with frequency ω and period $T = 2\pi/\omega$, and $\lambda \ll 1$. One tries to find solutions to the time-dependent Schrödinger equation (TDSE) $i\partial_t |\Psi(t)\rangle = \hat{H}(t) |\Psi(t)\rangle$ with nonzero λ , where $|\Psi(t)\rangle$ should

satisfy

$$|\Psi(T)\rangle = \hat{F}|\Psi(0)\rangle \quad (\text{B1})$$

with \hat{F} being the Floquet operator. When $\lambda = 0$, $|n(t)\rangle \equiv e^{-iE_n t}|n\rangle$ satisfies the TDSE $i\partial_t|n(t)\rangle = \hat{H}_s|n(t)\rangle$. When $0 < \lambda \ll 1$, one can expand $|\Psi(t)\rangle$ in the basis of $\{|n(t)\rangle\}$ as $|\Psi(t)\rangle = \sum_n c_n(t)e^{-iE_n t}|n\rangle$. Substituting it into the TDSE yields

$$c_n(t) = c_n(0) - i\lambda \sum_l \int_0^t c_l(t')e^{-i\Delta_{l,n}t'} V_{n,l}(t')dt', \quad (\text{B2})$$

where $\Delta_{l,n} = E_l - E_n$ is the energy difference between the states $|l\rangle$ and $|n\rangle$, and $V_{n,l}(t) = \langle n|\hat{H}_V(t)|l\rangle$ is the matrix elements of $\hat{H}_V(t)$ in the basis $\{|n\rangle\}$. When $\lambda \ll 1$, one can expand $c_n(t)$ in powers of λ as

$$c_n(t) = c_n^{(0)} + \lambda c_n^{(1)}(t) + \lambda^2 c_n^{(2)}(t) + O(\lambda^3). \quad (\text{B3})$$

Through substituting it into Eq. (B2) and comparing the coefficients before the k th order of λ of both sides of the equation, one can obtain the series of coefficients

$$\begin{aligned} c_n^{(1)}(t) &= c_n^{(1)}(0) - i \sum_l \int_0^t c_l^{(0)} e^{-i\Delta_{l,n}t_1} V_{n,l}(t_1) dt_1, \\ c_n^{(2)}(t) &= c_n^{(2)}(0) - i \sum_l \int_0^t c_l^{(1)}(t_1) e^{-i\Delta_{l,n}t_1} V_{n,l}(t_1) dt_1 \\ &= c_n^{(2)}(0) - i \sum_l \int_0^t c_l^{(1)}(0) e^{-i\Delta_{l,n}t_1} V_{n,l}(t_1) dt_1 - \sum_{l,m_1} \int_0^t \left[\int_0^{t_1} c_l^{(0)} e^{-i\Delta_{l,m_1}t_2} V_{m_1,l}(t_2) dt_2 \right] e^{-i\Delta_{m_1,n}t_1} V_{n,m_1}(t_1) dt_1, \\ &\dots \end{aligned} \quad (\text{B4})$$

Thus,

$$\begin{aligned} c_n(t) &= c_n^{(0)} + \lambda c_n^{(1)}(0) + \lambda^2 c_n^{(2)}(0) - i\lambda \sum_l \int_0^t [c_l^{(0)} + \lambda c_l^{(1)}(0)] e^{-i\Delta_{l,n}t_1} V_{n,l}(t_1) dt_1 \\ &\quad - \lambda^2 \sum_{l,m_1} \int_0^t \left[\int_0^{t_1} c_l^{(0)} e^{-i\Delta_{l,m_1}t_2} V_{m_1,l}(t_2) dt_2 \right] e^{-i\Delta_{m_1,n}t_1} V_{n,m_1}(t_1) dt_1 + O(\lambda^3) \\ &= c_n(0) - i\lambda \sum_l c_l(0) \int_0^t e^{-i\Delta_{l,n}t_1} V_{n,l}(t_1) dt_1 - \lambda^2 \sum_{l,m_1} c_l(0) \int_0^t \left[\int_0^{t_1} e^{-i\Delta_{l,m_1}t_2} V_{m_1,l}(t_2) dt_2 \right] e^{-i\Delta_{m_1,n}t_1} V_{n,m_1}(t_1) dt_1 + O(\lambda^3). \end{aligned} \quad (\text{B5})$$

Labeling the column vector $[c_1(t); c_2(t); \dots; c_{\mathcal{D}}(t)]$ as $|c(t)\rangle$ with \mathcal{D} being the total Hilbert space dimension, Eq. (B5) at $t = T$ can be written in the matrix form

$$|c(T)\rangle = [\hat{I} + \lambda \hat{F}_1 + \lambda^2 \hat{F}_2 + O(\lambda^3)]|c(0)\rangle, \quad (\text{B6})$$

where \hat{I} is the identity matrix and

$$\begin{aligned} \hat{F}_1 &= -i \sum_{n,l} \int_0^T e^{-i\Delta_{l,n}t_1} V_{n,l}(t_1) dt_1 |n\rangle\langle l|, \\ \hat{F}_2 &= - \sum_{n,l} \sum_{m_1} \int_0^T e^{-i\Delta_{m_1,n}t_1} V_{n,m_1}(t_1) \left[\int_0^{t_1} e^{-i\Delta_{l,m_1}t_2} V_{m_1,l}(t_2) dt_2 \right] dt_1 |n\rangle\langle l|. \end{aligned} \quad (\text{B7})$$

Writing Eq. (B1) in the matrix form

$$e^{-i\hat{E}T}|c(T)\rangle = \hat{F}|c(0)\rangle, \quad (\text{B8})$$

where $e^{-i\hat{E}T} = \text{diag}([e^{-iE_1 T} \ e^{-iE_2 T} \ \dots \ e^{-iE_{\mathcal{D}} T}])$, one can directly write down the Floquet operator

$$\hat{F} = e^{-i\hat{E}T} [\hat{I} + \lambda \hat{F}_1 + \lambda^2 \hat{F}_2 + O(\lambda^3)]. \quad (\text{B9})$$

The k th-order Floquet operator $\lambda^k \hat{F}_k$ can be viewed as the ‘‘photon’’ assisted transition between levels $|m_0\rangle$ and

$|m_k\rangle$, which is intermediated by $k-1$ levels $|m_i\rangle$ ($i = 1, 2, \dots, k-1$) in order. There can be single-photon resonance and multiphoton resonance during this k th-order transition. Expand each transition matrix element $V_{m_{i+1},m_i}(t)$ in the Fourier series as $V_{m_{i+1},m_i}(t) = \sum_{q_i} f_{q_i}(m_i, m_{i+1}) e^{iq_i \omega t}$, where q_i are integer numbers. Single-photon resonance between $|m_i\rangle$ and $|m_{i+1}\rangle$ happens in the condition that there exists a nonzero \tilde{q}_i making $\tilde{q}_i \omega = \Delta_{m_i, m_{i+1}}$. Multiphoton resonance between $|m_i\rangle$ and $|m_{i+p}\rangle$ ($p > 1$) happens in the condition that there exists a set of $\{\tilde{q}_i, \tilde{q}_{i+1}, \dots, \tilde{q}_{i+p-1}\}$ making $\Delta_{m_i, m_{i+p}} = (\tilde{q}_i + \tilde{q}_{i+1} + \dots + \tilde{q}_{i+p-1})\omega$ and there does not

exist any set of $\{\tilde{q}_i, \tilde{q}_{i+1}, \dots, \tilde{q}_{i+p'-1}\}$ making $\Delta_{m_i, m_{i+p'}} = (\tilde{q}_i + \tilde{q}_{i+1} + \dots + \tilde{q}_{i+p'-1})\omega$ for any $1 \leq p' < p$ at the same time. If \hat{F}_k contains q_r ($0 \leq q_r \leq k$) resonance processes, no matter if it is single-photon or multiphoton resonance, the integrals over time lead to a factor T^{q_r} . Thus, in a tight manner, if $\lambda T \ll 1$, one can expand the Floquet Hamiltonian in the Taylor series as

$$\begin{aligned} \hat{H}_F &= \frac{i}{T} \ln \{ e^{-i\hat{E}T} [\hat{I} + \lambda \hat{F}_1 + \lambda^2 \hat{F}_2 + O(\lambda^3)] \} \\ &= \hat{H}_\omega + \frac{i}{T} [\lambda \hat{F}_1 + \lambda^2 \hat{F}_2 - \frac{\lambda^2}{2} \hat{F}_1^2 + O(\lambda^3 T^3)], \quad (\text{B10}) \end{aligned}$$

$$\begin{aligned} \hat{H}_F^{(1)} &= \frac{i}{T} \ln e^{-i\hat{H}_{\text{on}}T} + J \left\{ \delta_{g,U} + \frac{u}{2} \delta_{|g-U|,\omega} + (1 - \delta_{g,U}) \frac{i[e^{-i(g-U)T} - 1]}{T} \right. \\ &\quad \times \left[\frac{1}{g-U} + \frac{u(1 - \delta_{|g-U|,\omega})(g-U)}{(g-U+\omega)(g-U-\omega)} \right] \left. \right\} \sum_j \hat{\mathcal{P}}_{j-1,j+2}^{(g-U)} \hat{c}_{j+1}^\dagger \hat{c}_j + \text{H.c.} \\ &\quad + J \left\{ \frac{i(e^{-igT} - 1)}{T} \left[\frac{1}{g} + \frac{u(1 - \delta_{g,\omega})}{2(g-\omega)} + \frac{u}{2(g+\omega)} \right] + \frac{u}{2} \delta_{g,\omega} \right\} \sum_j \hat{\mathcal{P}}_{j-1,j+2}^{(g)} \hat{c}_{j+1}^\dagger \hat{c}_j + \text{H.c.} \\ &\quad + J \left\{ \frac{i[e^{-i(g+U)T} - 1]}{T} \left[\frac{1}{g+U} + \frac{u(1 - \delta_{g+U,\omega})}{2(g+U-\omega)} + \frac{u}{2(g+U+\omega)} \right] + \frac{u}{2} \delta_{g+U,\omega} \right\} \hat{\mathcal{P}}_{j-1,j+2}^{(g+U)} \hat{c}_{j+1}^\dagger \hat{c}_j + \text{H.c.}, \quad (\text{B11}) \end{aligned}$$

where $\hat{\mathcal{P}}_{j-1,j+2}^{(g-U)}$, $\hat{\mathcal{P}}_{j-1,j+2}^{(g)}$, and $\hat{\mathcal{P}}_{j-1,j+2}^{(g+U)}$ are defined in Eq. (5). When we set $U = g$, the effective Floquet Hamiltonian is reduced to Eq. (6).

APPENDIX C: HILBERT SPACE FRAGMENTATION WITHOUT DRIVING

When $u = 0$, the Hamiltonian of the system reduces to $\hat{H}_0 = \hat{H}_{\text{on}} + J \sum_j (\hat{c}_j^\dagger \hat{c}_{j+1} + \text{H.c.})$. In the large tilting limit and at $U = g$, the effective Hamiltonian up to first order (using the Schrieffer-Wolff transformation [71]) is given by

$$\hat{H}_{u=0}^{\text{eff}} = J \sum_j \hat{\mathcal{P}}_{j-1,j+2}^{(0)} (\hat{c}_j^\dagger \hat{c}_{j+1} + \hat{c}_{j+1}^\dagger \hat{c}_j), \quad (\text{C1})$$

which is the same as Hamiltonian (7). Thus, for a long range of time, the Hilbert space will be split in the same way as that in Sec. III A.

To demonstrate this HSF of \hat{H}_0 in the large tilt limit, we study the EE dynamics, the fidelity dynamics, the saturated density profile, and the dynamics of the density autocorrelation function through exact diagonalization of the evolution operator $\hat{U}(t) = e^{-i\hat{H}_0 t}$ for $L = 16$ and large values of g . The results are shown in Fig. 7, in which all initial states are correspondingly the same as those in Figs. 2(b)–2(e). All observables show qualitatively similar behavior to that in Figs. 2(b)–2(e), thus signaturing the same HSF as that in Sec. III A.

where $\hat{H}_\omega = \frac{i}{T} \ln e^{-i\hat{E}T} = \text{diag}\{\text{mod}([E_1 \ E_2 \ \dots \ E_D], \omega)\}$ is the effective on-site potential obtained by folding the unperturbed energies into one Floquet Brillouin zone with width ω .

For our model, we treat $\hat{H}_J(t)$ as a perturbation to \hat{H}_{on} , assuming $J, uJ \ll g, U, \omega/2\pi$, and g and U are comparable. The eigenstates of \hat{H}_{on} are the Fock states $|\vec{n}\rangle = |n_0 n_1 \dots n_{L-2} n_{L-1}\rangle$ with eigenenergy $E_{\vec{n}} = U \sum_{j=0}^{L-2} n_j n_{j+1} - g \sum_{j=0}^{L-1} j n_j$, where $n_j = 0, 1$ denotes the particle number at the site j . Applying the TDPT introduced above, we can derive the first-order effective Floquet Hamiltonian

APPENDIX D: THE ODD-EVEN EFFECT OF PARTICLE NUMBER ON THE LARGEST KRYLOV SUBSPACE WHEN $\omega = \omega_2^*$

The spatial-reflection operator reflects the particles in a Fock state $|\vec{n}\rangle = |n_0 n_1 \dots n_{L-2} n_{L-1}\rangle$, such that $\hat{R}|\vec{n}\rangle = |n_{L-1} n_{L-2} \dots n_1 n_0\rangle \equiv |\underline{\vec{n}}\rangle$. It is easy to see that

$$\begin{aligned} \hat{\mathcal{P}}_{L-j-1, L-j+2}^{(2g)} \hat{c}_{L-j+1}^\dagger \hat{c}_{L-j} &= \hat{R} \hat{\mathcal{P}}_{j-1, j+2}^{(0)} \hat{c}_{j+1}^\dagger \hat{c}_j \hat{R}^{-1}, \\ \hat{\mathcal{P}}_{L-j-1, L-j+2}^{(2g)} \hat{c}_{L-j}^\dagger \hat{c}_{L-j+1} &= \hat{R} \hat{\mathcal{P}}_{j-1, j+2}^{(0)} \hat{c}_{j+1}^\dagger \hat{c}_j \hat{R}^{-1}. \quad (\text{D1}) \end{aligned}$$

Thus, corresponding to a nonzero $\langle \vec{l} | \hat{H}_{\omega_2^*}^{\text{eff}} | \vec{n} \rangle$, the matrix element $\langle \underline{\vec{l}} | \hat{H}_{\omega_2^*}^{\text{eff}} | \underline{\vec{n}} \rangle$ is also nonzero. It is obvious that if a Krylov subspace contains a pair of mutually reflected states $\{|\vec{n}\rangle, |\underline{\vec{n}}\rangle\}$ (including the case when $|\vec{n}\rangle$ is a reflection invariant state with $|\underline{\vec{n}}\rangle = |\vec{n}\rangle$), then all the Fock states in this Krylov subspace can be paired by the spatial reflection transformation. Otherwise, the Krylov subspace does not contain any pair of mutually reflected Fock states. Under spatial reflection, the Krylov subspace of the former kind is invariant, in the sense that the set of bases in the Krylov subspace does not change. The Krylov subspace of the latter kind will be transformed to its reflection partner.

Depending on the parity of the total particle number N , there may or may not exist a reflection-invariant Krylov subspace. The expectation values of \hat{e} in a Fock state $|\vec{n}\rangle$ and its reflected state read $e_{\vec{n}} = \langle \vec{n} | \hat{e} | \vec{n} \rangle = -\sum_j j n_j + \sum_j n_j n_{j+1}$ and $e_{\underline{\vec{n}}} = e_{\vec{n}} - 2 \sum_j j n_{L+1-j} + N(L+1)$, respectively. If N is odd, the parity of \hat{e} in the two states is opposite to each other, thus $|\vec{n}\rangle$ and $|\underline{\vec{n}}\rangle$ belong to different parity symmetry spaces. In this way, the Krylov subspaces in the even- and

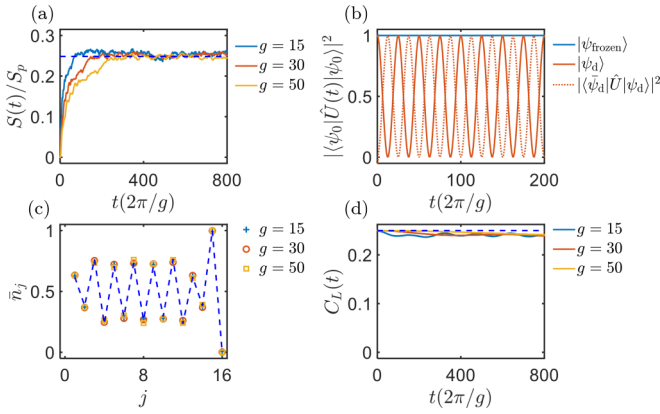


FIG. 7. (a) $S(t)/S_p$ vs time t (in units of $2\pi/g$) for $g = 15, 30$, and 50 . The blue dashed line denotes $S_p[\mathcal{K}_{\text{cdw1}}^{(0)}]/S_p$. (b) At $g = 50$, the fidelity dynamics from the frozen state $|\psi_{\text{frozen}}\rangle$ (blue line) and the domain state $|\psi_d\rangle$ (red line). The red dotted line shows the amplitude of state transfer from $|\psi_d\rangle$ to $|\bar{\psi}_d\rangle$. The oscillation period for state $|\psi_d\rangle$ is approximately π/J . (c) The saturated density profile \bar{n}_j for $g = 15, 30$, and 50 , which is averaged over time $t \in [700, 800] \frac{2\pi}{g}$ and all the initial Fock states in $\mathcal{K}_{\text{cdw1}}^{(0)}$. The blue dashed line denotes $n_j[\mathcal{K}_{\text{cdw1}}^{(0)}]$. (d) $C_L(t)$ vs time t (in units of $2\pi/g$) for $g = 15, 30$, and 50 . The blue dashed line denotes the lower bound $C_L^{(0)} = 0.25$. In (c) and (d), the data for all the values of g almost collapse with each other. In all plots, the initial states are the same as that in Figs. 2(b)–2(e) correspondingly, and the other parameters are $u = 0$ and $L = 16$. The energies are scaled in units of J .

odd-parity symmetry spaces are in one-to-one correspondence through the spatial-reflection transformation, and there is no reflection-invariant Krylov subspace. If N is even, the parity of \hat{e} in a pair of mutually reflected Fock states is the same, and there exist reflection-invariant Krylov subspaces. One such Krylov subspace is the one that contains the charge-density-wave state $|\text{CDW1}\rangle = |0101 \dots 01\rangle$ and its reflected partner $|\text{CDW2}\rangle = |1010 \dots 10\rangle$. Viewing four sites as a cell, both the sequences 0101 in $|\text{CDW1}\rangle$ and 1010 in $|\text{CDW2}\rangle$ can be changed to 0110 under the action of $\hat{H}_{\omega_2}^{\text{eff}}$. Thus, under $N/2$ times the action of $\hat{H}_{\omega_2}^{\text{eff}}$, both $|\text{CDW1}\rangle$ and $|\text{CDW2}\rangle$ can be coupled to the same state $|01100110 \dots 0110\rangle$, which is reflection-invariant. So, $|\text{CDW1}\rangle$ and $|\text{CDW2}\rangle$ are in the same Krylov subspace, and this subspace is reflection-invariant.

Numerically, we find that the largest Krylov subspace at all system sizes contains the charge-density-wave states. Thus, when N is odd, there are two largest Krylov subspaces in the half-filling sector, which lie in the even- and odd-parity symmetry space of \hat{e} , respectively. When N is even, there is only one largest Krylov subspace, which lies in the even-parity symmetry space and is reflection-invariant [note that

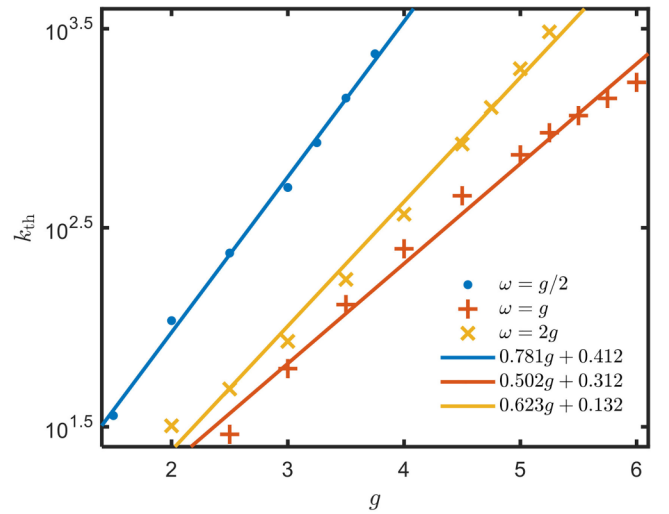


FIG. 8. The heating time k_{th} vs the tilting strength g at $\omega = g/2$ (blue dots), g (red pluses), and $2g$ (yellow crosses), starting from the charge-density-wave state $|\text{CDW1}\rangle$. The blue, red, and yellow lines are the corresponding fitting functions. The other parameters are $U = g$, $u = 1$, and $L = 20$.

$e_{m_{\text{cdw1}}} = -N(N-1)$ and $e_{m_{\text{cdw2}}} = -N^2$]. This odd-even effect leads to different fitting functions for quadruple and non-quadruple lattice sites.

APPENDIX E: THE PRETHERMAL TIME WINDOWS FOR THE THREE KINDS OF HSF

Due to the higher-order corrections, the system will thermalize if the evolution time is sufficiently long. For large values of g , the higher-order corrections are small, and the HSF studied in this work can survive for a long range of time. To show the long prethermal time for HSF, we study the thermalization time k_{th} as functions of g . We study the evolution from the charge-density-wave state $|\text{CDW1}\rangle$. k_{th} is defined as the number of driving cycles that are required for $S(kT)$ to reach the predicted thermalization value. To reduce the finite-size effect, we perform the simulation for $L = 20$ through the Krylov space-based algorithm [72] for our Hamiltonian $\hat{H}(t)$. Numerically, we determine k_{th} as $\min(\{k_c | S(kT)/S_p > 0.98, \forall k > k_c\})$.

In Fig. 8, we show k_{th} versus g at $\omega = g/2$, g , and $2g$ and $u = 1$. For the three cases, k_{th} increases exponentially with g , indicating that the HSF will exist for a long period of time. We also see that k_{th} increases the fastest at $\omega = g/2$ and the slowest at $\omega = g$. It is related to the degree of splitting of the Hilbert space. The number of Krylov subspaces is the highest for Hamiltonian (7) and the lowest for Hamiltonian (8).

[1] J. M. Deutsch, *Phys. Rev. A* **43**, 2046 (1991).
 [2] M. Srednicki, *Phys. Rev. E* **50**, 888 (1994).
 [3] M. Srednicki, *J. Phys. A* **32**, 1163 (1999).
 [4] M. Rigol, M. Dunjko, and V. Olshanii, *Nature (London)* **452**, 854 (2008).

[5] D. A. Abanin, W. D. Roeck, and F. Huveneers, *Ann. Phys.* **372**, 1 (2016).
 [6] R. Nandkishore and D. A. Huse, *Annu. Rev. Condens. Matter Phys.* **6**, 15 (2015).
 [7] D. A. Abanin, E. Altman, I. Bloch, and M. Serbyn, *Rev. Mod. Phys.* **91**, 021001 (2019).

- [8] S. Moudgalya, B. A. Bernevig, and N. Regnault, *Rep. Prog. Phys.* **85**, 086501 (2022).
- [9] T. Kinoshita, T. Wenger, and D. S. Weiss, *Nature (London)* **440**, 900 (2006).
- [10] M. Rigol, V. Dunjko, V. Yurovsky, and M. Olshanii, *Phys. Rev. Lett.* **98**, 050405 (2007).
- [11] A. Polkovnikov, K. Sengupta, A. Silva, and M. Vengalattore, *Rev. Mod. Phys.* **83**, 863 (2011).
- [12] M. Serbyn, Z. Papić, and D. A. Abanin, *Phys. Rev. Lett.* **111**, 127201 (2013).
- [13] D. A. Huse, R. Nandkishore, and V. Oganesyan, *Phys. Rev. B* **90**, 174202 (2014).
- [14] V. Ros, M. Müller, and A. Scardicchio, *Nucl. Phys. B* **891**, 420 (2015).
- [15] A. Chandran, I. H. Kim, G. Vidal, and D. A. Abanin, *Phys. Rev. B* **91**, 085425 (2015).
- [16] M. Schulz, C. A. Hooley, R. Moessner, and F. Pollmann, *Phys. Rev. Lett.* **122**, 040606 (2019).
- [17] E. van Nieuwenburg, Y. Baum, and G. Refael, *Proc. Natl. Acad. Sci. USA* **116**, 9269 (2019).
- [18] S. R. Taylor, M. Schulz, F. Pollmann, and R. Moessner, *Phys. Rev. B* **102**, 054206 (2020).
- [19] R. Yao and J. Zakrzewski, *Phys. Rev. B* **102**, 104203 (2020).
- [20] T. Chanda, R. Yao, and J. Zakrzewski, *Phys. Rev. Res.* **2**, 032039(R) (2020).
- [21] L. Zhang, Y. Ke, W. Liu, and C. Lee, *Phys. Rev. A* **103**, 023323 (2021).
- [22] R. Yao, T. Chanda, and J. Zakrzewski, *Phys. Rev. B* **104**, 014201 (2021).
- [23] Y.-Y. Wang, Z.-H. Sun, and H. Fan, *Phys. Rev. B* **104**, 205122 (2021).
- [24] Q. Guo, C. Cheng, H. Li, S. Xu, P. Zhang, Z. Wang, C. Song, W. Liu, W. Ren, H. Dong, R. Mondaini, and H. Wang, *Phys. Rev. Lett.* **127**, 240502 (2021).
- [25] W. Morong, F. Liu, P. Becher, K. S. Collins, L. Feng, A. Kyprianidis, G. Pagano, T. You, A. V. Gorshkov, and C. Monroe, *Nature (London)* **599**, 393 (2021).
- [26] C. J. Turner, A. A. Michailidis, D. A. Abanin, M. Serbyn, and Z. Papić, *Nat. Phys.* **14**, 745 (2018).
- [27] C. J. Turner, A. A. Michailidis, D. A. Abanin, M. Serbyn, and Z. Papić, *Phys. Rev. B* **98**, 155134 (2018).
- [28] W. W. Ho, S. Choi, H. Pichler, and M. D. Lukin, *Phys. Rev. Lett.* **122**, 040603 (2019).
- [29] M. Serbyn, D. A. Abanin, and Z. Papić, *Nat. Phys.* **17**, 675 (2021).
- [30] A. Chandran, T. Iadecola, V. Khemani, and R. Moessner, *Annu. Rev. Condens. Matter Phys.* **14**, 443 (2023).
- [31] S. Pai, M. Pretko, and R. M. Nandkishore, *Phys. Rev. X* **9**, 021003 (2019).
- [32] P. Sala, T. Rakovszky, R. Verresen, M. Knap, and F. Pollmann, *Phys. Rev. X* **10**, 011047 (2020).
- [33] V. Khemani, M. Hermele, and R. Nandkishore, *Phys. Rev. B* **101**, 174204 (2020).
- [34] S. Moudgalya, A. Prem, R. Nandkishore, N. Regnault, and B. A. Bernevig, Thermalization and Its Absence within Krylov Subspaces of a Constrained Hamiltonian, in *Memorial Volume for Shoucheng Zhang* (World Scientific, Singapore, 2021), Chap. 7, pp. 147–209.
- [35] S. Moudgalya and O. I. Motrunich, *Phys. Rev. X* **12**, 011050 (2022).
- [36] G. De Tomasi, D. Hetterich, P. Sala, and F. Pollmann, *Phys. Rev. B* **100**, 214313 (2019).
- [37] Z.-C. Yang, F. Liu, A. V. Gorshkov, and T. Iadecola, *Phys. Rev. Lett.* **124**, 207602 (2020).
- [38] C. M. Langlett and S. Xu, *Phys. Rev. B* **103**, L220304 (2021).
- [39] G. Francica and L. Dell’Anna, *Phys. Rev. B* **108**, 045127 (2023).
- [40] B. Mukherjee, Z. Cai, and W. V. Liu, *Phys. Rev. Res.* **3**, 033201 (2021).
- [41] B. Mukherjee, D. Banerjee, K. Sengupta, and A. Sen, *Phys. Rev. B* **104**, 155117 (2021).
- [42] S. Scherg, T. Kohlert, P. Sala, F. Pollmann, B. Hebbe Madhusudhana, I. Bloch, and M. Aidelsburger, *Nat. Commun.* **12**, 4490 (2021).
- [43] W.-H. Li, X. Deng, and L. Santos, *Phys. Rev. Lett.* **127**, 260601 (2021).
- [44] P. Frey, L. Hackl, and S. Rachel, *Phys. Rev. B* **106**, L220301 (2022).
- [45] T. Kohlert, S. Scherg, P. Sala, F. Pollmann, B. Hebbe Madhusudhana, I. Bloch, and M. Aidelsburger, *Phys. Rev. Lett.* **130**, 010201 (2023).
- [46] S. Ghosh, I. Paul, and K. Sengupta, *Phys. Rev. Lett.* **130**, 120401 (2023).
- [47] S. Aditya and D. Sen, *SciPost Phys. Core* **6**, 083 (2023).
- [48] K. Lee, A. Pal, and H. J. Changlani, *Phys. Rev. B* **103**, 235133 (2021).
- [49] D. Hahn, P. A. McClarty, and D. J. Luitz, *SciPost Phys.* **11**, 074 (2021).
- [50] A. Morningstar, V. Khemani, and D. A. Huse, *Phys. Rev. B* **101**, 214205 (2020).
- [51] C. Pozderac, S. Speck, X. Feng, D. A. Huse, and B. Skinner, *Phys. Rev. B* **107**, 045137 (2023).
- [52] A. Eckardt, *Rev. Mod. Phys.* **89**, 011004 (2017).
- [53] S. Greschner, L. Santos, and D. Poletti, *Phys. Rev. Lett.* **113**, 183002 (2014).
- [54] F. Meinert, M. J. Mark, K. Lauber, A. J. Daley, and H.-C. Nägerl, *Phys. Rev. Lett.* **116**, 205301 (2016).
- [55] H. Zhao, J. Knolle, and F. Mintert, *Phys. Rev. A* **100**, 053610 (2019).
- [56] H. Zhao, J. Vovrosh, F. Mintert, and J. Knolle, *Phys. Rev. Lett.* **124**, 160604 (2020).
- [57] W. Liu, Y. Ke, B. Zhu, and C. Lee, *New J. Phys.* **22**, 093052 (2020).
- [58] A. Soori and D. Sen, *Phys. Rev. B* **82**, 115432 (2010).
- [59] A. Sen, D. Sen, and K. Sengupta, *J. Phys.: Condens. Matter* **33**, 443003 (2021).
- [60] D. N. Page, *Phys. Rev. Lett.* **71**, 1291 (1993).
- [61] L. Vidmar and M. Rigol, *Phys. Rev. Lett.* **119**, 220603 (2017).
- [62] L. Herviou, J. H. Bardarson, and N. Regnault, *Phys. Rev. B* **103**, 134207 (2021).
- [63] Z. Guo, B. Liu, Y. Gao, A. Yang, J. Wang, J. Ma, and L. Ying, *Phys. Rev. B* **108**, 075124 (2023).
- [64] D. Barredo, S. de Léséleuc, V. Lienhard, T. Lahaye, and A. Browaeys, *Science* **354**, 1021 (2016).
- [65] M. Endres, H. Bernien, A. Keesling, H. Levine, E. R. Anschuetz, A. Krajenbrink, C. Senko, V. Vuletic, M. Greiner, and M. D. Lukin, *Science* **354**, 1024 (2016).
- [66] A. Browaeys, D. Barredo, and T. Lahaye, *J. Phys. B* **49**, 152001 (2016).

- [67] D. Barredo, V. Lienhard, S. de Léséleuc, T. Lahaye, and A. Browaeys, *Nature (London)* **561**, 79 (2018).
- [68] A. Browaeys and T. Lahaye, *Nat. Phys.* **16**, 132 (2020).
- [69] T.-H. Yang, B.-Z. Wang, X.-C. Zhou, and X.-J. Liu, *Phys. Rev. A* **106**, L021101 (2022).
- [70] A. Omran, H. Levine, A. Keesling, G. Semeghini, T. T. Wang, S. Ebadi, H. Bernien, A. S. Zibrov, H. Pichler, S. Choi, J. Cui, M. Rossignolo, P. Rembold, S. Montangero, T. Calarco, M. Endres, M. Greiner, V. Vuletić, and M. D. Lukin, *Science* **365**, 570 (2019).
- [71] S. Bravyi, D. P. DiVincenzo, and D. Loss, *Ann. Phys.* **326**, 2793 (2011).
- [72] Y. Saad, *SIAM J. Numer. Anal.* **29**, 209 (1992).